



UNIVERSITÀ
DEGLI STUDI
DI PADOVA

Università degli Studi di Padova

DIPARTIMENTO DI FISICA E ASTRONOMIA

Corso di Laurea in Astronomia

Millimeter observations of Young Stellar Objects with the CARMA interferometer

Candidato:

Marco Zennaro

Matricola 617390

Relatori:

Prof. Alberto Franceschini

Dott. Luca Ricci

Contents

1	Young Stellar Objects and Protoplanetary Disks	5
1.1	Classification	6
1.2	Disk Structure	9
1.2.1	Active and Passive Disks	9
1.2.2	The Razor-Thin Approximation	9
1.2.3	Flared Disks	11
1.2.4	Two-Layer Disk	12
1.3	Assumptions and Uncertainties	14
2	Interferometry	17
2.1	Young's Slits and Principles of Interferometry	17
2.2	Modern Astronomical Interferometry	18
2.2.1	The (u,v) plane	19
2.2.2	Primary Beam and Wavelength Ranges	21
2.3	Calibration of Interferometric Data	22
2.4	Deconvolution and Cleaning	24
2.4.1	CLEAN	24
3	CARMA Data for Young Disks in the Serpens Region	27
3.1	Serpens Star Forming Region	27
3.2	CARMA Interometer	31
3.3	Data Reduction	32
3.3.1	Raw Data Presentation	32
3.3.2	Data Calibration and Editing	32
3.3.3	Making the Map	47
3.3.4	Photometry with Casaviewer	49
4	Results	53
4.1	Data Analysis	53
4.2	Relations Between Disk and Stellar Properties	55
5	Conclusions	63
	Bibliography	65

Chapter 1

Young Stellar Objects and Protoplanetary Disks

In this chapter I will give a brief presentation of protoplanetary disks. In sect. 1.1 I will present the classification of Young Stellar Objects and its evolutionary meaning, in sect 1.2 I will overview different models for the disk structure and in the last section I will explain the source of uncertainties and the other assumptions I made in my Thesis.

Observations indicate that stars are formed out of molecular clouds, typically giant molecular clouds with masses of order $10^5 M_{\odot}$. Star formation starts when a perturbation disrupts the pressure equilibrium and causes the cloud (or part of it) to collapse under its self gravity.

If this collapsing region has non-zero initial angular momentum, always happening in astrophysics, part of the material (dust and gas), will not fall directly into the central core (where the star will form), but, because of the conservation of angular momentum, it will form a disk around it. At a certain radius, the centrifugal force will balance the gravitational attraction; this radius is known as the *circularization radius* and can be estimated to be around $\sim 10^2 - 10^3$ AU. At this point some of the material, via different methods, but essentially due to viscous stresses, loses its angular momentum and falls into the central core whilst other part moves outward to conserve the total disk momentum. In the above described scenario, in the end we will have, a central (accreting) core that will give birth to a star, but right now is still a protostar, with a disk around it.

Observational evidence for the presence of dust and gas around these Young Stellar Objects (YSOs) exists since many years from a variety of different tracers, like optical emission line spectra (Herbig, 1950), optical absorption of background emission (Ricci et al., 2008), continuum excess in the infrared (Ney et al., 1973) and sub-mm (Beckwith et al., 1990). The real morphology, however, could only be revealed in the 1990s with the use of the Hubble Space Telescope in the optical (O'Dell and Wong, 1996) and

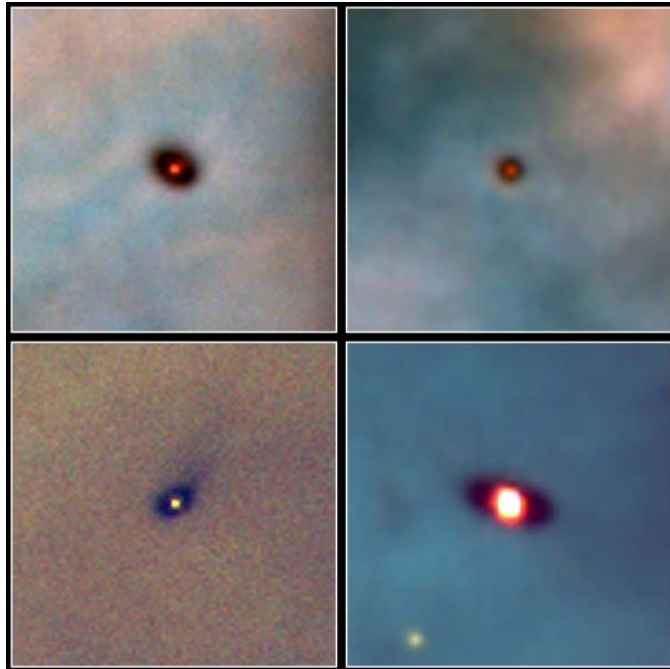


Figure 1.1: One of the first images of protoplanetary disks, obtained in the Orion Nebula with the Hubble Space Telescope (From McCaughrean & O'Dell, 1995)

with the IRAM Plateau de Bure Interferometer in the millimeter (Dutrey et al., 1996). High resolution imaging revealed flattened structures interpreted as disks seen in projection in the plane of the sky. Few cases show a disk exactly face-on, i.e. with the symmetry axis oriented along the line of sight, but more often the disk axis forms a non-zero angle with the line of sight, and the projected image is more flattened because of the inclination. Also, in some cases, high angular resolution observations of molecular lines, especially CO rotational transitions in the millimeter, provided evidence for velocity gradients along the disk. Data collected by Simon Dutrey and Guilloteau (2000) suggest that the disks are in Keplerian motion around the central star.

1.1 Classification

YSOs have been observed in several star forming regions, with different Spectral Energy Distributions (SED). These objects have been classified according to the slope of the SED in the infrared region of the spectrum (Lada and Wilking, 1984; André et al., 1993; André and Montemerle, 1994), usu-

ally defined by the parameter

$$\alpha_{IR} \equiv \frac{\Delta \log(\lambda F_\lambda)}{\Delta \log \lambda}. \quad (1.1)$$

Conventions vary but typically α_{IR} is measured by fitting the observations that span a wavelength range between the near infrared (often at $\sim 2.2\mu m$) and the mid-infrared (usually at $\sim 20\mu m$).

YSOs have been divided in four classes (as shown in fig 1.2):

Class 0: they are not visible at wavelengths shorter than $\sim 10 - 20\mu m$ and have a steeply rising spectrum in the mid-to-far IR.

Class I: the SED of these objects is approximately flat or rising at near and mid infrared wavelengths but not as steep as Class 0 objects: $\alpha_{IR} \geq -0.3$

Class II: their SED falls in the visible region and they have an IR SED that decreases with wavelength but still in excess in respect to a single temperature black body curve. This is the class of classical T Tauri stars, named like this after the prototype T Tauri, which was recognized as being part of an interesting class of variable stars that, later, were found to have a protoplanetary disk around them. For this Class $-1.6 \leq \alpha_{IR} < -0.3$

Class III: the YSOs of this Class show no, or very little, infrared excess, hence the SED is essentially that of a stellar photosphere with $\alpha_{IR} < -1.6$.

The classification above is made on empirical observations, but it is by now entwined with a theoretical interpretation as an evolutionary sequence (Adams et al., 1987): Class 0 YSOs are identified with the first step of the life of a protostar with the collapse of the molecular dense cloud still happening, and this idea is confirmed by the fact that any protostar present in the center is not visible even in the near infrared wavelengths as we would expect from a source embedded in a thick cloud. The first class of objects in which a disk is recognizable is the Class I. These YSOs are still surrounded in an envelope of infalling material but the fact that they are visible in the near IR tells us that the envelope is thinner than for the Class 0 YSOs. In the Class II stage the circumstellar envelope has been dissipated, the SED can now be modeled as a sum of a, now, optically visible star and the emission in the IR (where the disk emission is optically thick) and mm (where it is optically thin) from a surrounding circumstellar disk. In the Class III stage there is little or no evidence for the circumstellar disk, they are still pre-Main Sequence stars, some of them display evidence for surrounding debris disks made of asteroid/comet-sized objects, and a population of smaller dust grains generated by impacts between the larger objects. In my Thesis I will present the analysis on data at mm wavelengths obtained for a sample of Class II YSOs.

8CHAPTER 1. YOUNG STELLAR OBJECTS AND PROTOPLANETARY DISKS

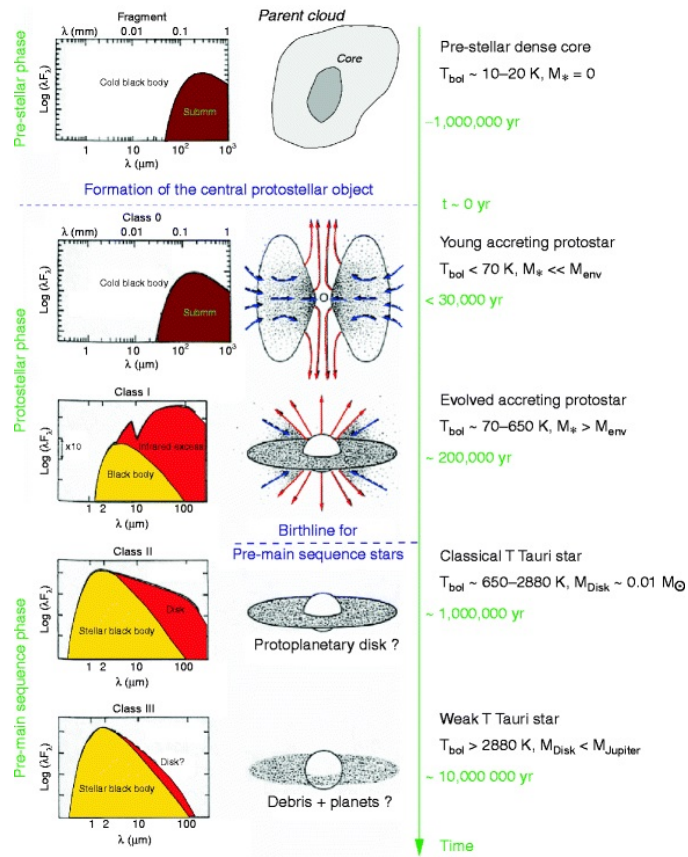


Figure 1.2: Classification of YSOs and evolutionary interpretation. From Andr  2002

1.2 Disk Structure

1.2.1 Active and Passive Disks

The first main classification that can be done for disks is whether they are active or passive. In passive disks the main heating process is the absorption and re-emission of the radiation coming from the star, while in active disks heating is due to the dissipation of gravitational potential energy, as matter in the disk spirals in towards the star. In each case the heating per unit area drops off with increasing radius from the star. If the disk extends out to large enough radii, heating due to the ambient radiation field provided by nearby stars can become significant and prevent the disk temperature from dropping below some level; for normal star forming environments this temperature threshold is about $\sim 10 - 20K$.

The relative importance of these two methods of heating depends: on the accretion rate and the amount of intercepted radiation. Infalling matter will radiate an amount of energy per unit mass that is approximately given by gravitational potential at the stellar surface: GM_*/R_* , here G is gravitational constant, M_* is the mass of the star and R_* it's the star radius. The disk will absorb a fraction $f < 1$ of the total radiation originated by the star. To make a rough estimate we can take $f = 1/4$, which is correct for a flat, razor-thin disk. In this case the accretion rate \dot{M} above which accretional heating dominates can be crudely evaluated as

$$\frac{GM_*\dot{M}}{R_*} = \frac{1}{4}L_*, \quad (1.2)$$

where the quantities with $*$ are referred to the central star, M is the mass and L is the luminosity. For a young Solar mass star with luminosity $L_* = L_\odot = 3.9 \times 10^{33} \text{ergs}^{-1}$ and a radius of $R_* = 2R_\odot$

$$\dot{M} \approx 2 \times 10^{-8} M_\odot \text{yr}^{-1}.$$

Accretion rates measured for classical T Tauri stars, (Gullbring et al., 1998) range from an order of magnitude above this limit to two order of magnitude below, so it would be oversimplifying to treat protoplanetary disks as only passive or active. Instead when accretion is stronger, which is achieved in the early stages of the disk evolution, the disk will be active hence dominated by the internal heating while in later phases the reprocessing of the stellar radiation dominates and the disk will become passive. For the Class II YSOs, analyzed in my Thesis, we can consider their disks as passive.

1.2.2 The Razor-Thin Approximation

In the last section I used the *flat, razor-thin* model to get an estimate the absorption, of a passive disk, when the accretional heating dominates. This

is the simplest approximation for disk structure: a razor-thin disk in the equatorial plane that completely absorbs the radiation coming from the star and re-emits it locally as a single temperature blackbody.

In this scenario, we can consider a surface in the plane of the disk at distance r from a star of radius R_* , assumed to be a constant sphere of constant brightness I_* . We need a set of polar, spherical, coordinates such that the axis of the coordinate system points to the center of the star, the stellar flux passing through this surface is

$$F = \int I_* \sin \theta \cos \phi d\Omega, \quad (1.3)$$

where $d\Omega$ represents the element of solid angle. Let's consider only the top half of the star only and equate that to the radiation from only the top surface of the disk, this means imposing an energy equilibrium between absorbed and emitted radiation so an equilibrium between heating and cooling. The limits of integration are therefore

$$\begin{aligned} -\frac{\pi}{2} < \phi \leq \frac{\pi}{2} \\ 0 < \theta \leq \sin^{-1}\left(\frac{R_*}{r}\right). \end{aligned}$$

Substituting $d\Omega = \sin \theta d\theta d\phi$ into the integral for the flux becomes

$$F = I_* \int_{-\frac{\pi}{2}}^{\frac{\pi}{2}} \cos \phi d\phi \int_0^{\sin^{-1}\left(\frac{R_*}{r}\right)} \sin^2 \theta d\theta, \quad (1.4)$$

which gives the result

$$F = I_* \left[\sin^{-1}\left(\frac{R_*}{r}\right) - \left(\frac{R_*}{r}\right) \sqrt{1 - \left(\frac{R_*}{r}\right)^2} \right]. \quad (1.5)$$

For a star with effective temperature T_* , the brightness is given by $I_* = \left(\frac{1}{\pi}\right)\sigma T_*^4$ where σ is the Stefan-Boltzmann constant (Ribicky & Lightman, 1979). Equating F to the one-sided emission of the disk σT_{disk}^4 , assumed to be a Black-Body, we obtain a radial temperature profile

$$\frac{T_{disk}(r)}{T_*} = \frac{1}{\pi} \left[\sin^{-1}\left(\frac{R_*}{r}\right) - \left(\frac{R_*}{r}\right) \sqrt{1 - \left(\frac{R_*}{r}\right)^2} \right]. \quad (1.6)$$

To see that the factor 1/4 adopted in the previous section in eq. (1.2) is correct, we can integrate this equation over all disk radii to obtain the disk total luminosity

$$L_{disk} = 2 \times \int_{R_*}^{\infty} 2\pi r T_{disk}^4 dr = \frac{1}{4} L_*. \quad (1.7)$$

The form of the temperature profile given by eq. (1.6) becomes more clear if we expand the right-hand-side in a Taylor series in the limit $(R_*/r) \ll 1$, meaning far away from the stellar surface, in this case we obtain

$$T_{disk} \propto r^{-3/4}. \quad (1.8)$$

1.2.3 Flared Disks

Multi-wavelength observations of disks have been used to derive some of the main properties of young circumstellar disks (Duchene, 2008). In the optical, small particles (sizes $< 1\mu m$) scatter efficiently the radiation from the star, so optical images at high angular resolution can be used to probe the geometrical structure of the disk surface. These images have revealed a “flared” structure, meaning a structure with an increasing height, over the equatorial plane of the disk, the further away from the central star hinting that the razor-thin model was indeed an over-simplified approximation.

Another proof for the need of a new model was given by observations in the infrared. In this wavelength regime the disk thermal emission is optically thick and therefore reflects the emitting temperature of the disk surface. Assuming a simple power-law for the temperature radial profile $T(r) \sim r^{-q}$, the infrared SED of young T Tauri stars are best-fitted usually with $q \approx 1/2$, different from the $q = 3/4$ found in eq. (1.8), again disagreeing with the hypothesis of a razor-thin disk.

Kenyon & Hartmann (1987) proposed a model based on flared disks with an optically thin disk atmosphere directly heated by the stellar radiation. Starting from eq. (1.3) the temperature profile can be computed integrating that equation over the part of the stellar surface visible from the disk at radius r . Here I will present an approximate treatment valid for $r \gg R_*$ and consider the star to be a point source of radiation¹. At a distance r from the star the radiation is absorbed by the disk at height h_p ; in the frame of our approximation, the angle between the incident radiation and the local disk surface is given by

$$\alpha = \frac{dh_p}{dr} - \frac{h_p}{r}. \quad (1.9)$$

The rate of heating per unit disk area at distance r is

$$Q_+ = 2\alpha \left(\frac{L_*}{4\pi r^2} \right), \quad (1.10)$$

the factor 2 comes from the fact that the disk has two sides and all of the stellar surface is visible from the surface of the disk. Assuming a black body

¹as found in the book “Astrophysics of planet formation” by Philip J. Armitage (Cambridge University press). For the exact calculation see Kenyon and Hartmann, 1987, “Spectral energy distribution of T Tauri star: disk flaring and limits of accretion”.

radiation emitted by the disk

$$Q_- = 2\sigma T_{disk}^4. \quad (1.11)$$

Now equating (1.10) and (1.11) we obtain

$$T_{disk}(r) = \left(\frac{L_*}{4\pi\sigma} \right)^{1/4} \alpha^{1/4} r^{-1/2}. \quad (1.12)$$

Knowing that $L_* = 4\pi R_*^2 \sigma T_*^4$ we can rewrite eq. 1.12 as

$$\frac{T_{disk}}{T_*} = \left(\frac{R_*}{r} \right)^{1/2} \alpha^{1/4}. \quad (1.13)$$

Therefore at a large radii we expect a temperature profile going as

$$T_{disk} \propto r^{-1/2}, \quad (1.14)$$

in full agreement with observations. A flared disk cools slower than a flat one, in the radial direction, because it absorbs, at the same radius, more radiation from the star.

1.2.4 Two-Layer Disk

Thus far we only probed the external structure of the disk, assuming that the intercepted stellar radiation is re-radiated as a single temperature black body. To better investigate the interior of the disk we need observations at longer wavelengths. In the millimeter region the emission is optically thin, since it is less probable that this, lower energy radiation, is absorbed in respect to the IR wavelengths, and can be used to probe the cold internal and dense regions in the mid-plane of the outer disk. Since those regions contain most of the disk mass, a measured integrated flux in the millimeter can be converted into an estimate for the disk mass. The local emission from the disk is then the result of a composition between a cool blackbody, from the interior, and a warmer one, from the disk surface.

In these models (Chiang and Goldreich, 1997; Dullemond et al., 2001), the disk surface layer absorbs the energy from stellar radiation, heating up and re-emitting half of the energy outward and half inward, i.e. towards the disk interior. The interior layer absorbs part of this re-emitted radiation, heats up, and in turn re-emits radiative energy away from the disk. The temperature in the surface, T_s , and in the interior, T_i , are computed by imposing hydrostatic equilibrium.

Once the thermal structure of the disk is determined, we can compute the total dust emission summing the flux contributions from the surface and the interior; for the interior layer:

$$F_\nu^i = \frac{2\pi \cos i}{d^2} \int_{R_{in}}^{R_{out}} B_\nu[T_i(R)] [1 - e^{-\tau_\nu^i(R)}] R dR, \quad (1.15)$$

and for the surface:

$$F_{\nu}^s = \frac{2\pi}{d^2} \int_{R_{in}}^{R_{out}} B_{\nu}[T_s(R)][1 + e^{-\tau_{\nu}^i(R)}] \Delta\Sigma(R) \kappa_{\nu}^s R dR. \quad (1.16)$$

In Eq (1.15) and (1.16), ν is the frequency, i is the disk inclination, d is the distance, R_{in} and R_{out} are the inner and outer radii, respectively, $\Delta\Sigma$ is the dust surface density in the disk surface, κ_{ν}^s is the dust opacity in the surface layer, (in this model κ_{ν}^s is considered radially constant) τ_{ν}^i is the line of sight dust optical depth in the interior, i.e.

$$\tau_{\nu}^i = \frac{\Sigma(R) \kappa_{\nu}^i}{\cos i}, \quad (1.17)$$

where $\Sigma(R)$ is the radial profile of the dust surface density, κ_{ν}^i is the dust opacity in the disk interior; finally, $B_{\nu}[T_s(R)]$ and $B_{\nu}[T_i(R)]$ are the Planck function at temperature T :

$$B_{\nu} = \frac{2h\nu^3}{c^2} \frac{1}{e^{\frac{h\nu}{k_B T}} - 1}, \quad (1.18)$$

where h is the Planck constant, c is the speed of light, and k_B is the Boltzmann constant.

At sub-millimeter wavelengths most of the disk mass is contained in optically thin regions, i.e. with $\tau_{\nu}^i \ll 1$ and F_{ν}^i can be approximated as

$$F_{mm}^i \approx \frac{2\pi}{d^2} \int_{R_{in}}^{R_{out}} B_{mm}[T_i(R)] \Sigma(R) \kappa_{mm}^i R dR, \quad (1.19)$$

where B_{mm} is the Planck function at sub-millimeter wavelengths. Considering that at all radii $\Sigma(R) \gg \Delta\Sigma(R)$, the comparison between Eq.(1.19) and (1.16) shows that the disk mid-plane dominates the emission at sub-mm wavelengths. From Eq. (1.19) it follows that the surface brightness of the disk at millimetric wavelengths is

$$I_{mm} \approx B_{mm}[T_i(R)] \Sigma(R) \kappa_{mm}^i. \quad (1.20)$$

Sub-mm observations, with enough angular resolution to spatially resolve the disk emission, in combination with a disk model which can derive the temperature profile $T_i(R)$ and dust opacity κ_{mm}^i , can be used to constrain the radial profile of the dust surface density $\Sigma(R)$. The first extensive interferometric survey of protoplanetary disks in the millimeter was done by Dutrey et al. (1996); they observed, at 2.7 mm with the Plateau de Bure Interferometer, 33 circumstellar disks in Taurus-Auriga. In this survey the surface density profile $\Sigma(R)$ was modeled as a simple truncated power law:

$$\Sigma(R) = \begin{cases} \Sigma(R_0) \times \left(\frac{R}{R_0}\right)^{-p} & \text{for } R \leq R_{out} \\ 0 & \text{for } R > R_{out} \end{cases} \quad (1.21)$$

where R_0 is an arbitrary radius in the disk. They found values for R_{out} in the range between 50 and 300 AU.

Kitamura et al. (2002), observed at 2 mm a sample of 13 young disks with a better angular resolution, 1" (vs the 2-3" angular resolution obtained by Dutrey). For all the sources they constrained both the outer radius and the power-law index p within intervals of about, respectively 80 - 400 AU and 0 - 1.8. They also adopted a more realistic and physically motivated model for the radial profile of the surface density with an exponential taper:

$$\Sigma(R) = \Sigma(R_c) \times \left(\frac{R}{R_c}\right)^{-\gamma} \exp\left[-\left(\frac{R}{R_c}\right)^{2-\gamma}\right], \quad (1.22)$$

where R_c is a characteristic radial scale for this surface density profile and γ controls the radial variation of the surface density itself.

With this information it is possible to integrate Eq.(1.19). Assuming a model for the dust emission, from the observed frequency of the emission ν_{obs} it is possible to obtain the characteristic temperature of the dust, i.e. the temperature is now independent from the radius. This step is fundamental because by doing so B_{mm} in eq. (1.19) becomes independent from R and it can be taken out of the integral:

$$F = \frac{B_{mm}}{d^2} \int_{R_{in}}^{R_{out}} \kappa_{mm}^i 2\pi R \Sigma(R) dR. \quad (1.23)$$

Adopting a model for κ_{mm}^i , even this term can be placed out of the integral and it is easy to notice that what remains, $\int_{R_{in}}^{R_{out}} 2\pi R \Sigma(R) dR$, is the total dust mass, M_{dust} , of the disk. We have obtained the relation:

$$F = \frac{B_{mm} \kappa_{mm}^i M_{dust}}{d^2}. \quad (1.24)$$

From this equation we can infer the mass of the dust present in the disk, since with our observations we can measure the flux of the disk.

1.3 Assumptions and Uncertainties

As derived in section 1.2.3, for a passive, flared disk $T_{disk} \propto r^{-1/2}$ where T_{disk} is the dust temperature, one could ask if it is not an oversimplification to assume a temperature independent from the radius in the computation of Eq. (1.23). In fact, closer to the star, the dust temperature is indeed higher, generating larger values for the Planck function than in the outer disk; but a careful reader would remember that the protoplanetary disks are "flared" structures, meaning that at higher radii the h_p increases, and so does the the mass of the dust enclosed in a $r + \Delta r$ ring. Therefore the total

emission of a disk at mm wavelengths is dominated by dust emitting at 20K with an error of $\pm 10\text{K}$.

A more important source of uncertainty is represented by the dust opacity coefficient, κ_ν , the errors in the computation of this coefficient can be easily wrong by factors of 3 or 4. This uncertainty arises from the many assumptions one has to make in order to derive a model for it, like the dust grain size distribution, the grains' morphology and chemical structure which are all unknowns.

In my Thesis I will work on observations of disks at a wavelength of 3mm, therefore I will investigate only the dust properties. Hence the masses that I will infer will be dust masses; to obtain an upper limit for the disk total mass the canonical $M_{gas}/M_{dust} = 100$ can be used, even though this ratio is a good estimate only in the interstellar medium (ISM).

Chapter 2

Interferometry

In this chapter I will give an overview of interferometry and how it is applied nowadays in astronomy. I will start with the basic concepts in sect. 2.1 and then I will explain how they are still useful for modern astronomical interferometers in sect. 2.2. In sect. 2.3 I will describe the calibration process of the data and in the last section I will explain the processes used to obtain the final image.

2.1 Young's Slits and Principles of Interferometry

The beginning of interferometry can be set with the Thomas Young's double slit experiment performed in 1801. This experiment consisted (Fig. 2.1) of a single point source, emitting coherent radiation, the light coming from the source illuminates a plate pierced by two parallel slits, and is finally collected on a screen. Young observed interference fringes with constructive and destructive patterns observed as the delay of the two interfering rays changed. The separation of the fringes is given by λ/d where λ is the wavelength of the light and d is the distance between the slits. The fringe visibility is defined as the difference between maximum and minimum intensity, as measured on the screen, normalized by the sum of maximum and minimum intensity.

If the source is wider, we can think of it as a sequence of point sources each emitting radiation in a non-correlated manner. The image of the fringes on the screen, in this case, will be the sum of the interferences of each point. Since an angular displacement in the source produce the same displacement in the fringe pattern, as the source angular dimension approaches λ/d the fringes disappear into constant illumination, meaning that the visibility drops to 0. On the other hand, when the angular dimension of the source is $\ll \lambda/d$, hence much smaller than the angular resolution of the interferometer, the fringe visibility is 1.

Changes are observed also when the distance d between the slits is varied, for the same source. Decreasing this distance produces "washing out" of the

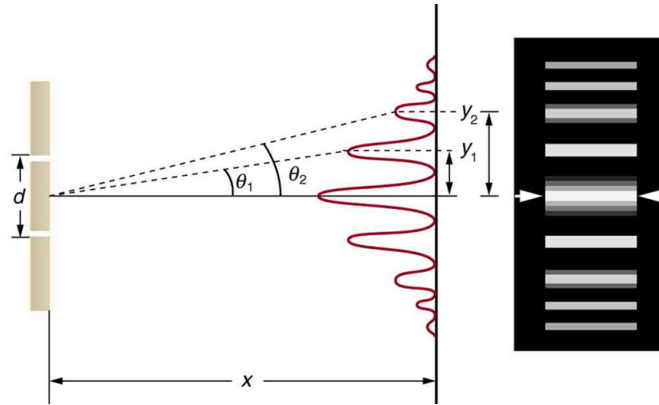


Figure 2.1: Young double slit experiment diagram

fringes, because the same displacement in the source means now much less shifting in the fringes pattern as a fraction of the fringes separation λ/d . In short, the smaller the distance the larger the source that can be probed. For small sources the visibility remains high out to large slit distances while for large sources the visibility of the fringes drops to zero quickly for increasing slit separation.

The relation between $I(\theta)$ and $V(d)$, respectively source brightness as a function of angular distance and visibility of interference fringes as a function of slit separation, is one that transforms a small Gaussian into a large Gaussian and vice versa, it can be demonstrated that this relation is a Fourier transform.

2.2 Modern Astronomical Interferometry

The situation described in the precedent section find very useful applications for astronomical observations. In Fig. 2.2 we can see a plane wave, from a source at infinity, as sampled by two telescopes, which are separated by a distance \mathbf{B} ; the path delay of the light here is given by $\mathbf{B} \cdot \mathbf{s}$ where \mathbf{s} is the unit vector in the direction of the source, and the phase delay is given by $k\mathbf{B} \cdot \mathbf{s} = 2\pi/\lambda$.

Consider a point source. We can call E the electric field registered by the first telescope; the one measured by the second, therefore, will be $E^{ik\mathbf{B} \cdot \mathbf{s}}$, for the effects of the delay in the phase. By electronically multiplying the two signals, or in the case of optical signals, using a Michelson or Fizeau system to combine the beams, we obtain an analogous combination as in the Young's experiment.

Even in this astronomical case, the source is never really a point, so we have to add the different fringe patterns produced by the different points

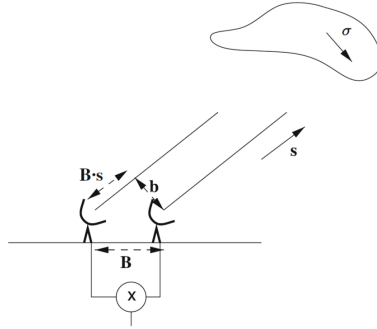


Figure 2.2: Basic diagram of an interferometer with baseline vector \mathbf{B} observing a source in a direction with unit vector \mathbf{s} (from Jackson, 2008 *Principles of Interferometry*)

which make up the source, in this way we obtain the response R of the interferometer as

$$R = \int I(\sigma) e^{ik\mathbf{B}(s+\sigma)} d\sigma, \quad (2.1)$$

where $(s + \sigma)$ is in the direction of the correspondent part in the source with intensity $I(d\sigma)$. σ is parallel to the projected baseline \mathbf{b} (Fig 2.2), $\mathbf{B} \cdot \sigma = \mathbf{b} \cdot \sigma$, so we have

$$R = e^{ik\mathbf{B} \cdot \mathbf{s}} \int I(\sigma) e^{ik\mathbf{b} \cdot \sigma} d\sigma. \quad (2.2)$$

The $e^{ik\mathbf{B} \cdot \mathbf{s}}$ term is dependent only on the array geometry and so can be removed from the integral. At this point we have a series of fringes, whose amplitude is given by the Fourier transform of the source intensity distribution. To get rid of the fringes in optical interferometer delay lines are used to compensate for the path difference and in radio interferometer with the use of electronic delays. After this step we are left only with the Fourier transform response which conveys information on the source surface brightness.

2.2.1 The (u,v) plane

To better analyze the Fourier transform in both its phase and amplitude, we can decompose both \mathbf{b} and σ in Cartesian coordinates. σ being a vector in the plane of the sky is easily decomposed in $\sigma = \sigma_x \mathbf{i} + \sigma_y \mathbf{j}$, with \mathbf{i} in the east-west direction and \mathbf{j} in the north-south direction. Keeping the same idea we can also decompose \mathbf{b} in $u\mathbf{i}$ and $v\mathbf{j}$ so that $\mathbf{b} \cdot \sigma = ux + vj$. The response can therefore be written as:

$$R = \int \int I(x, y) e^{2\pi i(ux+vj)} dx dy, \quad (2.3)$$

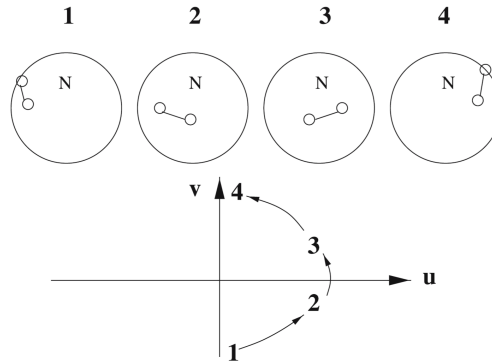


Figure 2.3: Schematic diagram showing the baseline between two telescopes as the Earth rotates. The E-W and N-S components of this vector give u and v (from Jackson, 2008 *Principles of Interferometry*).

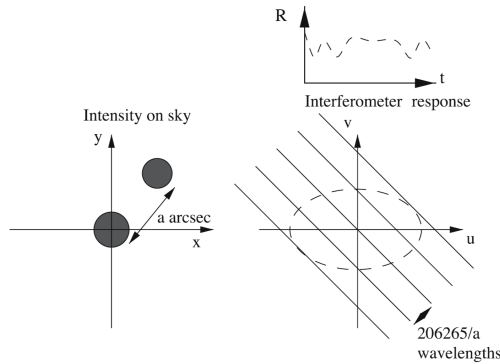


Figure 2.4: Diagram showing the interferometer response as a function of u and v for a double source on the sky (from Jackson, 2008 *Principles of Interferometry*).

where u and v are in units of wavelength, R is often referred to as the visibility function and can be found written as $V(u, v)$. The decomposition of \mathbf{b} can be explained by imagining to be sitting on the source and looking at the projected baseline, this would now appear as a straight line drawn onto earth (Fig 2.3). This line can be decomposed into a line parallel to the equator at its nearest point to the source and a component parallel to the line from this point to the north pole. These components are u and v and they change as the Earth rotates, tracing an ellipse, on the (u, v) plane, during a full rotation.

Fig 2.4 shows the basic Fourier transform relation in the case of a double source in the sky. A double source of angular separation of 1 radian produces stripes in the u, v plane of 1 wavelength, a double source of separation a arcsec would give a stripes of distance $d = 206265/a$ wavelengths. Super-

posed to this there is the ellipse-shaped track which represents the points of the (u, v) plane sampled during the observation with a single pair of antennas (or telescopes); over a day there are variations in the response as the interferometer follows the elliptical track over these stripes. Studying this variation in amplitude and phase, over the period of the observations, we can work backwards to deduce the separation and orientation on the stripes, and, by taking the Fourier transform, recover the source structure. The u, v track has a semimajor axis in the direction u of $\frac{L}{\lambda} \sin \delta$, and a semiminor axis in the v direction of $\frac{L}{\lambda} \sin \delta \sin D$, where L is the baseline length, D in the declination of the source and δ is the declination of the baseline, meaning the declination of the point in the sky to which the baseline vector points. The angular resolution which a baseline is capable to provide is given by the inverse of the maximum extent of the u, v ellipse, namely $\frac{\lambda}{L}$. If many baselines are present more measurements can be taken simultaneously, and the u, v plane is therefore more filled, hence it is easier to obtain a faithful reproduction of the sky intensity distribution in an interferometric image.

2.2.2 Primary Beam and Wavelength Ranges

Let's think back to the Young experiment. In this configuration, if the slits are widened the aperture distribution no longer consists of two delta functions, but of two delta functions convolved with a single wide slit. From the convolution theorem it follows that the interference pattern, being the Fourier transform of the aperture distribution, consists of the original two-slit fringe pattern multiplied by the Fourier transform of a wide slit, that is a *sync* function. The *sync* function has a width inversely proportional to the width of the slits (w), and the fringes disappear at delays greater than the width of the *sync* function $\frac{L}{w}$.

In an interferometer going away from the center of the field of view just corresponds to a different delay from that obtained at the center; the width of the slits translates directly to the aperture size of each interferometer element, and the field of view in radians is the wavelength of the light being studied divided by the diameter of the elements.

Again as in the case of Young's slits, we have to face the problem that the radiation is not monochromatic. We can consider different wavelengths separately and add each diverse fringe patterns, the separation between each maxima is λ/d . The result is that in the center of the fringe pattern, full-visibility fringes are seen, since there the delay is zero. At larger values of delay, further up in the screen, the interference fringes from different colors adds in such a way to reduce the visibility proportionally to the distance from the center even for a point source.

This effect at large delays translates directly for the interferometer in which a range of wavelengths causes a loss of the response at the edge of the field of view. If the bandwidth is $\Delta\lambda$, then the field of view is given by the beam

size divided by the fractional bandwidth

$$\Delta\sigma = \left(\frac{\lambda}{\Delta\lambda}\right) \left(\frac{\lambda}{L}\right). \quad (2.4)$$

To achieve reasonable signal-to-noise modern interferometer use a large fractional bandwidth, this means a very restricted field of view, a solution to this problem is to divide the signal in different channel and correlate them separately.

2.3 Calibration of Interferometric Data

As always, like with in any other observational technique in astronomy, we have to deal with the atmosphere. The light that traveled to us as a nearly perfect plane wave is disrupted by Earth's atmosphere, in the last microsecond, introducing phase, and at some wavelengths even amplitude, variation in the wavefront over small spatial, and potentially time, scales.

Furthermore, even without the atmospheric turbulences, the instrument response is never as the ideal one, so also this difference in the response has to be corrected through the calibration process.

It is now clear that what we observe is not the actual emitted $I^{true}(u, v)$ but a $I^{obs}(u, v)$ that is "corrupted" by the atmosphere and the instrument. The aim of the whole calibration process is to get rid of the atmosphere induced variations. This, of course, is not an easy task and usually is done in three steps: passband, flux and gain(or phase). For each of the previous calibration steps we have to make the assumption that

$$V_{ij}^{true}(u, v) = g_{ij} V_{ij}^{obs}, \quad (2.5)$$

where V_{ij} is measured by the baseline between the i and j antenna, and that

$$g_{ij} = g_i g_j \quad (2.6)$$

meaning that g_{ij} depends on the single antennas and not only on the baseline. With our calibrations we want to determine the g_{ij} terms which depend on both time and frequency; in order to do so we observe objects which properties are known and by dividing the theoretical value by the observed one we obtain the corrective term which can be then used to calibrate the data.

Passband Calibration

Since we have to deal with a band of wavelength instead of just only one, the first step in the calibration process is the Passband calibration. In short, we want to know how the response of the interferometer varies with the wavelengths $\Delta\lambda$ or the frequencies $\Delta\nu$, divided in windows and channels,

used in the observations. This is done by observing a known source, which is required to be sufficiently bright to be clearly detected by the interferometer in each frequency channel and that its brightness is constant over the interval of frequencies of the observations.

Unfortunately the scenario that occurs is almost never the one in which the observed response is the same of the theoretical one. In fact, while the calibrator has approximately a constant signal, over the interval of frequencies, what the instrument measures is a curve which has, in the first and last channels of the passband, signal equal to 0. The next step is to confront the two responses, in both phases and amplitudes, to determine the corrective term dependent on the frequency $g_{ij}(\nu)$. The passband calibrator is usually observed only once and at the beginning of the track, since the passband calibration does not need a mean value of the amplitudes and phases.

Gain Calibration

Since both phases and amplitudes show variation over a time interval, due to changes in the atmospheric condition or variation of the instrument response, we have to calibrate them over time.

Even in this step we want to observe a bright object, usually a quasar, but in addition we want it to be close to the source that we are going to observe in the track. In this way we are more sure that we will base the correction on something that will, probably, experience the same atmospheric turbulences as the target of interest of the observation. What is done, practically, is to observe for 2-3 minutes the calibrator every time it is possible, e.g. in between each observation of the research source, so that it is possible to know the variations in phase and amplitude for each baseline and during the whole time of the track.

With this information, and assuming that the spectrum of the calibrator is always the same, it is possible to determine the correction to apply to the data during the intervals between one observation of the calibrator and the other: $g_{ij}(t)$.

Flux Calibration

All of the previous calibrations steps still work with the raw observed phases and amplitudes, with the flux calibration we translate measured amplitudes in fluxes. As usual we want to observe a bright enough object and, in this case, we want it compact as well. The reason behind this request is because we do not want to resolve it with our interferometer, otherwise the visibility function measured by the interferometer will be a *sinc* like function where the representative flux of the object is only obtained close to the central peak in the (u, v) plane. If there is no other choice but to use a resolved object then only fluxes within 30 – 40% of the central peak are usually considered

for the calibration process.

For an unresolved flux calibrator, instead, the visibility function is uniform and we have more data to confront with the known flux of the calibrator.

2.4 Deconvolution and Cleaning

Even after the calibration process, we are still left with one major problem: the interferometer response has not been measured in the entire (u, v) plane. This means that the number of different images consistent with the data is infinite, since the unmeasured parts in the (u, v) plane could be filled in an infinite amounts of ways. The basic problem is that we want the image $V(x, y)$ resulting from the the full response function $V(u, v)$,

$$V(x, y) = \int \int V(u, v) e^{2\pi i(ux+vy)} dudv, \quad (2.7)$$

but, instead, we have the “dirty” image,

$$V_D(x, y) = \int \int V(u, v) S(u, v) e^{2\pi i(ux+vy)} dudv, \quad (2.8)$$

where $S(u, v)$ is the sampling function, which is 1 in the sampled regions of the (u, v) plane, and 0 elsewhere. Using the convolution theorem on the right-hand side of eq. (2.6) we can write

$$V_D(x, y) = V(x, y) * B(x, y), \quad (2.9)$$

where

$$B(x, y) = \int \int S(u, v) e^{2\pi i(ux,vy)} dudv \quad (2.10)$$

is called the “dirty beam”, which is the Fourier transform of the sampling function. The dirty beam is made of side lobes; this side lobes generate artifacts in the dirty image. Through the deconvolution we want to get rid of this artifacts. The image is obtained by doing the inverse Fourier transform of the visibility function V convolved with the dirty beam.

2.4.1 CLEAN

Recovering the image $I(x, y)$ is a deconvolution problem, in order to resolve it more information is needed. One of the possible ways to do so, and the way I used in my analysis is via the CLEAN algorithm.

The first step is to find the brightest point in the dirty map, shifting the dirty beam to this point and then scaling and subtracting off the dirty beam (or in loop a fraction of it). This scaling and subtracting the dirty beams goes on until the so called “residual” map consists only of noise. At this point the subtracted fluxes are convolved with a restoring beam and added

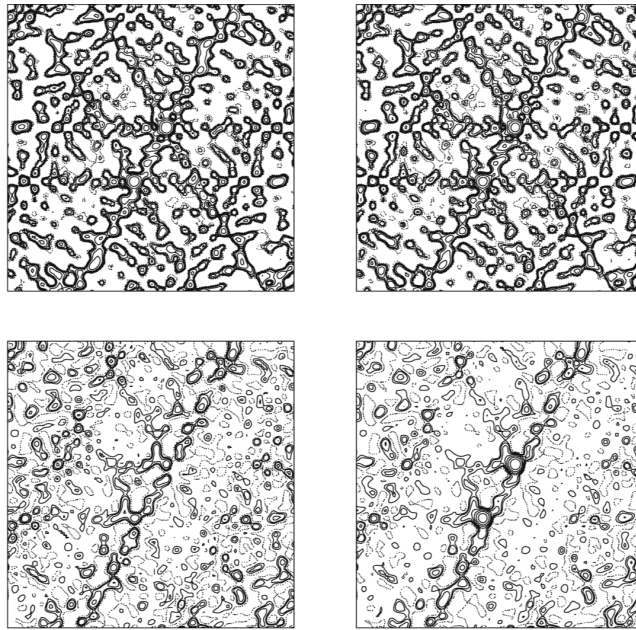


Figure 2.5: CLEANing procedure applied to a radio source consisting of two point source components observed with the VLA. All maps are contoured at the same level: (Top left) the dirty map; (Top right) the residual map after 10 iterations of CLEAN, in which a small amount of flux has been removed at each iteration; (Bottom left) the residual map after 100 iterations of CLEAN: note the removal of most of the dirty beam structure; (Bottom right) the CLEAN map after some further CLEANing, formed by the addition of the point source components back into the final residual map (from Jackson, 2008 *Principles of Interferometry*).

back into the field of noise to give the final “cleaned map” from which the side lobes of the dirty beam have been removed.

The restoring beam is a Gaussian which fits the central region of the dirty beam but without the side lobes. The final product is, therefore, an image, with the same angular resolution of the original, CLEANed from the side lobes of the dirty beam. The additional information that has been supplied to the deconvolution problem by CLEAN is the assumption that the sky consists of a finite number of point sources or alternatively that most of the sky is empty. Not surprisingly, therefore, CLEAN works very well for simple sources, but can occasionally fail on very large amorphous sources of low surface brightness.

Chapter 3

CARMA Data for Young Disks in the Serpens Region

In this chapter I will present the data editing I performed for a sample of 81 Young protoplanetary disks.. In the first section, I will give an introduction and a literature review of the Serpens star-forming region, in which the 81 disks I analyzed are located. In the second section I will give an overview of the CARMA interferometer, the instrument used by L. Ricci to record the data. In third section I will present the whole data calibration and imaging process: from the raw data to the final cleaned maps, and finally the measure of the flux of each disk.

3.1 Serpens Star Forming Region

The Serpens Molecular Cloud is a massive star forming region situated in the southern part of the Serpens Cauda constellation. It is a very young region, with stellar ages estimated from 1 to 3 Myr (Olivera, 2012), distant 415 ± 15 pc (Olmi & Testi, 2002) and covering more than 10deg^2 on the sky, as mapped by optical extinction measurements (Cambrèsy, 1999). This region can be divided into two subregions: Serpens Main and Serpens South (Fig 3.1 and 3.2 respectively).

The Serpens Main region first attracted the attention of Strom because of a very red bipolar-shaped nebulosity located several arcminutes west of S68 (Sharples, 1959). Since then, a considerable amount of work has been dedicated to the Serpens molecular cloud. It was soon recognized (Strom et al., 1974) as an active site of star formation and over 20 infrared sources were detected, several of them with SEDs compatible with those expected from pre-main-sequence stars (PMS) (Strom et al., 1976)

CO , NH_3 , HCO and H_2CO molecular radio observations have been carried out by several groups (Loren et al., 1979,1981; Loren and Wooten, 1980; Ho and Barret 1980; Rodriguez et al., 1980; Little et al., 1980; Ungerechts

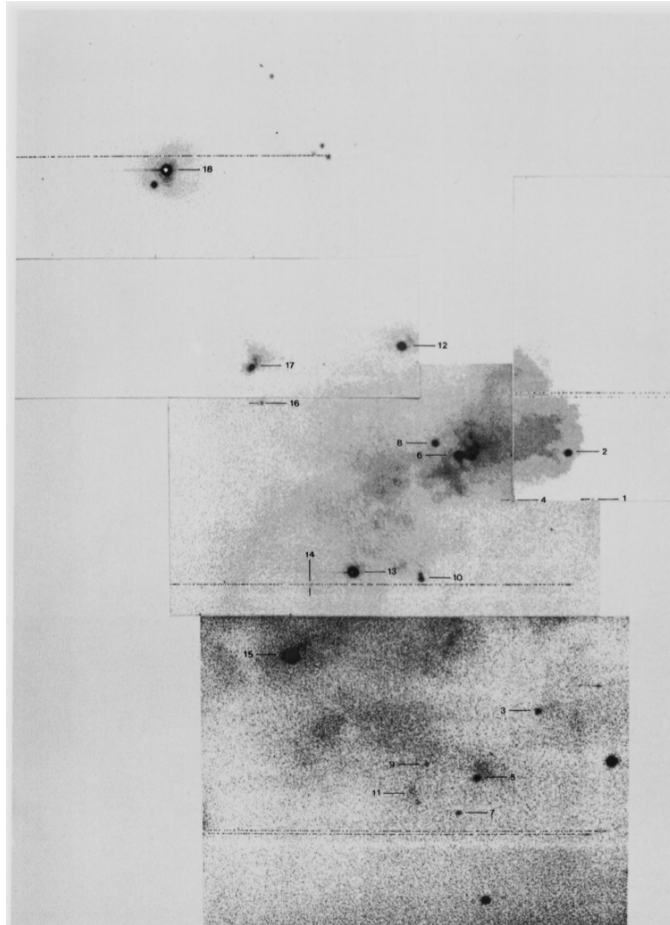


Figure 3.1: Image, in the I band ($\lambda = 9140\text{\AA}$), of the Serpens region from Gomez de Castro et al., (1988)



Figure 3.2: Image of the Serpens South region. This Spitzer picture is composed of three images taken with the telescope's Infrared Array Camera (IRAC) at 3.6 (blue), 4.5 (green), and 5.8 (red) microns. (NASA/JPL-Caltech/L. Allen (Harvard-Smithsonian CfA), Gould's Belt Legacy Team).

and Gusten, 1984). These observations showed that this region is a large molecular cloud where low-mass star-forming processes are taking place.

Serpens South is a nearby embedded cluster, recently discovered by Gutermuth et al. (2008) using the Spitzer Space telescope. The accurate distance to Serpens South remains unknown. Most of the literature studies adopt the same distance as the Serpens Cloud Core, i.e. 415 ± 15 pc, located about 3° north, because the YSOs associated with Serpens South have the same LSR velocities as the Serpens Cloud Core. From the Spitzer IRAC observations, Gutermuth et al. (2008) revealed that the cluster contains about 60 Class I protostars and 40 Class II sources. Recently, Bontemps et al. (2010) have discovered 7 Class 0 candidates in this region through the Herschel Gould Belt Survey (see André et al. 2010). In the central part of the cluster, the fraction of Class I protostars relative to all the YSOs (Class I/II) reaches about 80 % at the high surface density of $430 pc^{-2}$. These observations indicate that Serpens South is undoubtedly in the very early stage of cluster formation, i.e., Serpens South is a “protocluster” that is forming a number of stars. Gutermuth et al. (2008) also estimated the median projected distance between nearest neighbor YSOs to be about 3700 AU, significantly shorter than the typical length of protostellar outflow lobes, implying that the outflows can potentially influence star formation in this region.

The Serpens Molecular Cloud has been imaged by Spitzer as part of the cores to disks (c2d) program. The detected sources in the IRAC and MIPS bands were published by Harvey et al. (2006) and Harvey et al. (2007b), respectively. By combining the data in all bands, Harvey et al. (2007a) could identify a red population classified as YSO candidates, which is interpreted as being due to emission from the disk. Confirmation of their nature as young object members of the cloud was done through spectroscopy.

Recently Olivera et al. (2013) presented a study of the spectral energy distribution of 94 young stars surrounded by disks in the Serpens molecular cloud based on the photometry and Spitzer/IRS spectra. They found that the T Tauri stars in Serpens do not have a clear separation in fractional disk luminosities for different disk geometries: both flared and flat disks present wider, overlapping distributions.

For my analysis I used CARMA data, taken by L. Ricci, of 81 disks in the Serpens Molecular Cloud, previously observed by the Spitzer c2d program and further analyzed by Olivera (2009,2010,2013). The observations were made at 3mm to investigate the dust continuum emission of the disks. The difference between CARMA data and Spitzer data is that Spitzer works in the infrared, therefore it measures only the optically thick radiation; while with observations in the millimeter wavelength range it is possible to estimate the dust mass in the disk using the optically thin radiation.



Figure 3.3: Image with all the different types of antennas of the CARMA interferometer. Photo by Jens Kaufmann at <http://www.astro.caltech.edu/research/carma/>.

3.2 CARMA Interometer

CARMA (Combined Array for Research in Millimeter-wave Astronomy) was an astronomical interferometer consisting of six 10.4-meter, nine 6.1-meter, and eight 3.5-meter antennas used in combination to image the astronomical universe at millimeter wavelengths. Located on a high-altitude site in the Inyo Mountains of California, the array could be operated at three atmospheric bands: 1cm (27-35 GHz), 3mm (85-116 GHz) and 1mm (215-270 GHz) and can achieve an angular resolution as high as 0.15 arcseconds (from <http://www.astro.caltech.edu/research/carma/>). According to the CARMA observatory catalog, the median height of all telescope pads was at an elevation of 2196 m (7205 ft).

CARMA was initially created through the merger of the Owens Valley Radio Observatory (OVRO) Millimeter Array and the Berkeley-Illinois-Maryland Association (BIMA) Array. The Owens Valley Array was built and operated by Caltech in the Owens Valley near Big Pine, California. It consisted of six 10.4-meter telescopes. The BIMA Array was started by the University of California Berkeley with three 6.1-meter telescopes and expanded over the years to nine telescopes with the addition of the University of Illinois at Urbana-Champaign and the University of Maryland as partners. The BIMA Array was located at the Hat Creek Radio Observatory in northern California. In 2004, the two groups, in cooperation with the National Science Foundation, agreed to merge the two arrays into a single array on a higher site, the current Cedar Flat location. The merger involved moving the an-

tennas from their respective locations and the creation of completely new hardware and software array infrastructure. The construction and commissioning took roughly three years. The array began routine science operation in January 2007. The University of Chicago joined CARMA in the summer of 2008, adding eight 3.5-meter antennas to CARMA. These antennas were initially operated as an independent array, and had been integrated with the other fifteen antennas to form a single array.

The array could be configured in 5 different ways: A 0.25 - 2 km, B 100 - 1000 m, C 30 - 350 m, D 11 - 150 m, E 8 - 66 m; the numbers represent respectively the shortest and longest baseline in that configuration (data from <https://www.mmarray.org/>). For the data I analyzed configurations C and D were used.

3.3 Data Reduction

3.3.1 Raw Data Presentation

The data for this survey were collected, using the CARMA interferometer in 35 different tracks or “observing blocks”, between 03/24/2014 and 05/27/2014. The first 16 tracks were observed in the CARMA C configuration, the other 19 in the D configuration. In every observation 16 spectral windows were used, each with a bandwidth of 487.500 MHz and 39 channels. The central frequency used was 100 GHz ($\lambda=3\text{mm}$)

For the data editing and to create the maps I used MIRIAD; to retrieve the RMS in each map and the fluxes of the sources I used CASA; finally I used IDL to convert the measured fluxes into masses and to create the graphs that I will show in chapter 4.

All the other parameters of the observations can be found in table 3.1 in the next page.

3.3.2 Data Calibration and Editing

The beginning of the editing of interferometric data is the inspection of the quality of the data. This is because an interferometer is a very sophisticated system made of several parts which may give problems, and produce data points with clear anomalies throughout the observations.

The script I used had already some automatic editing, e.g. for the shadowing (when an antenna is covered by the shadow from another one) or for the edge channels (the 4 channels at the beginning and at the end of each spectral window).

The first check is on the system temperatures (T_{sys}). In order to do so I checked the plots T_{sys} vs time looking for high points in the graphs, like in Fig 3.4, and then, in case of anomalies, searched for a confirmation using the MIRIAD command *listobs*. *listobs* is a command that gives all the technical

Table 3.1: Table showing the observation details

Obsblock ID (c1219)	Date (2014)	Disk ID	Calibrators
IC_100Serpen.1	03-24	1,70,80,131	F:MWC349 G:1743-038 B:3C454.3
IC_100Serpen.2	03-28	131,145,139,120,114	F:MWC349 G:1743-038 B:3C454.3
IC_100Serpen.3	03-29	114,98,52,62	F:MWC349 G:1743-038 B:3C454.3
IC_100Serpen.6	04-01	55,41	F:MWC349 G:1743-038 B:3C453.3
IC_100Serpen.7	04-04	41,6,38,58,89,130	F:MARS G:1743-038 B:1337-129
IC_100Serpen.8	04-04	130,36,119,66,113,148	F:MARS G:1743-038 B:1337-129
IC_100Serpen.9	04-06	148,9,14,20,29,32	F:MARS G:1743-038 B:1337-129
IC_100Serpen.10	04-07	32,43,54,60	F:MWC349 G:1743-038 B:3C454.3
IC_100Serpen.11	04-08	60,65,69	F:MWC349 G:1743-038 B:3C454.3
IC_100Serpen.12	04-09	69,71,76	F:MWC349 G:1743-038 B:1337-129
IC_100Serpen.13	04-11	76,81,83	F:MARS G:1743-038 B:1337-129
IC_100Serpen.14	04-11	83,87	F:MWC349 G:1743-038 B:3C454.3
IC_100Serpen.15	04-15	87,96	F:MWC349 G:1743-038 B:3C454.3
IC_100Serpen.16	04-18	96,103,105,111	F:MWC349 G:1743-038 B:3C454.3
1D_100Serpen.1	05-02	116,123,125,136	F:MWC349 G:1743-038 B:1927+739
1D_100Serpen.3	05-05	136,147,149,24,90,129,3	F:MARS G:1743-038 B:1337-129
1D_100Serpen.4	05-06	3,7,10	F:MWC349 G:1743-038 F:1927+739
1D_100Serpen.7	05-06	10,15	F:NEPTUNE G:1743-038 B:3C454.3
1D_100Serpen.8	05-07	130,36,119,66,113,148	F:MWC349 G:1743-038 B:1927+739
1D_100Serpen.9	05-09	53,59,124,61,64,75	F:MWC349 G:1743-038 B:1927+739
1D_100Serpen.10	05-10	75,82,86	F:MWC349 G:1743-038 B:1927+739
1D_100Serpen.11	05-17	86,88,92,97	F:MWC349 G:1743-038 B:1927+739
1D_100Serpen.12	05-20	3,7,97,100	F:MWC349 G:1743-038 B:1927+739
1D_100Serpen.13	05-21	104,106,115	F:MWC349 G:1743-038 B:1927+739
1D_100Serpen.14	05-22	104,106,115	F:MWC349 G:1743-038 B:1927+739
1D_100Serpen.15	05-23	104,106,115,122,127	F:MWC349 G:1743-038 B:1927+739
1D_100Serpen.16	05-24	127,137,142,146	F:MARS G:1743-038 B:1337-129
1D_100Serpen.17	05-25	146,13,40	F:MWC349 G:1743-038 B:1337-129
1D_100Serpen.18	05-26	40,109	F:MWC349 G:1743-038 B:1927+739
1D_100Serpen.19	05-27	109,10,59,111,30	F:MWC349 G:1743-038 B:1337-129

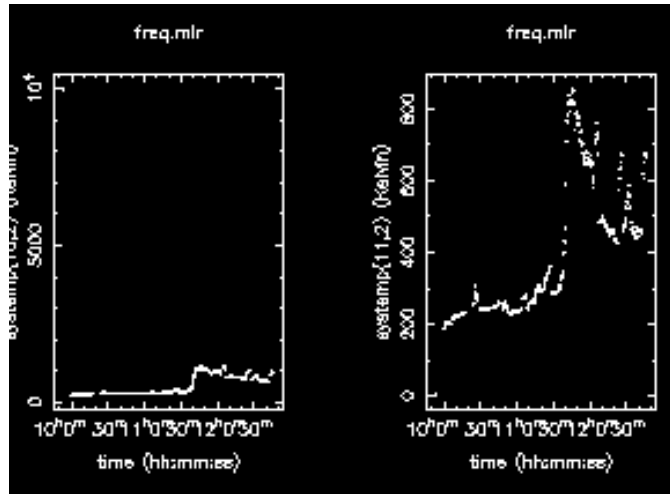


Figure 3.4: Examples of bad T_{sys} . The image shows the T_{sys} vs time plot for the 10-12 and 11-12 baseline From track 1D.14. In both at a certain point the T_{sys} starts to increase excessively.

informations of the track, such as the list of the observed objects with the time, local and universal, and the system temperatures. After this double check, on both the Miriad graphs and the *listobs* command, all the time intervals with high T_{sys} were flagged, that is removed through the command *uvflag* from the original data set. *uvflag* is used to change flags corresponding to visibility data. If flagval equals “flag”, the uv data are flagged as bad, i.e. removed; for flagval equal to “unflag”, the uv data are flagged as good, i.e. kept.

After the checking of the T_{sys} , I looked, for each track, at the raw amplitudes and phases, for each baseline, during the whole track. This is important because, even if not calibrated, they can reveal hints that there will still be problem after the calibration. Examples of anomalies in the data are phase or amplitude jumps, as shown in Fig 3.5 and 3.6. In the first case there is a clear difference in the measured phase of the calibrator between the fifth and sixth observation, but before and after everything is coherent, so, in this case, only the data took in the interval between these two are to be removed. In the second the fourth measure of the calibrator amplitude shows a clear anomaly in respect with the others, and since it is not known when, between the third and fifth observation the anomaly started and ended, all the data between the third and fifth calibrator measurement are to be flagged.

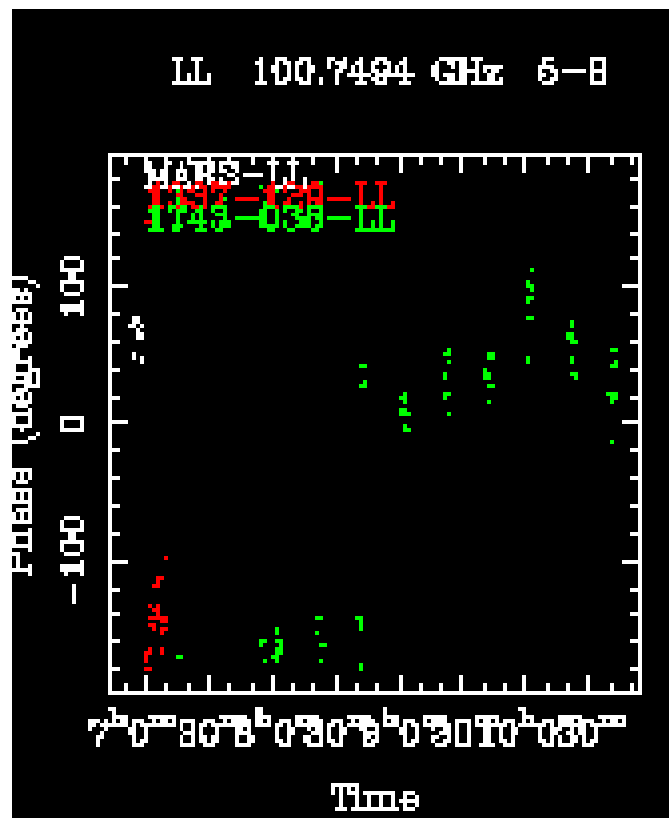


Figure 3.5: Example of s phase jump, in the middle of the track. This image shows the Phase vs Time plot for the raw data of the calibrators.

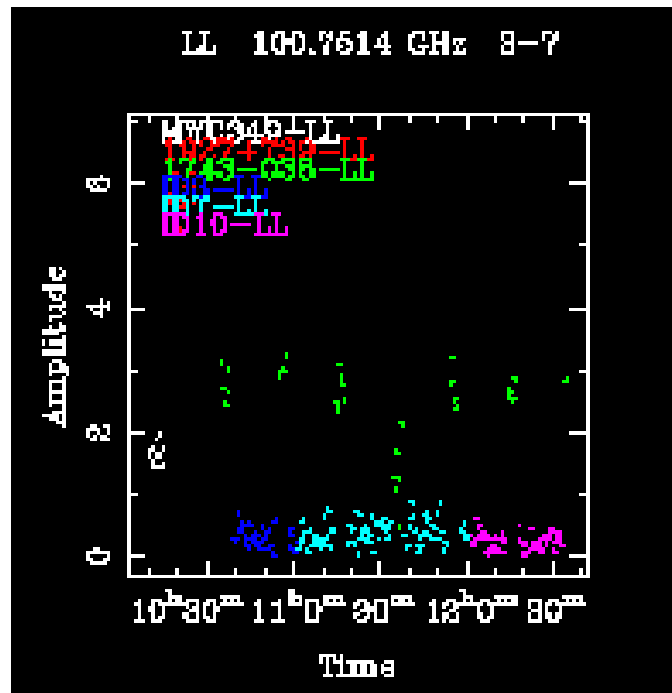


Figure 3.6: Example of non-optimal raw amplitudes, a jump can be seen for the amplitude of the gain calibrator which should be constant during the track. This image shows the Amplitude vs Time plot for the raw data of the calibrators measured by the 3-7 baseline.

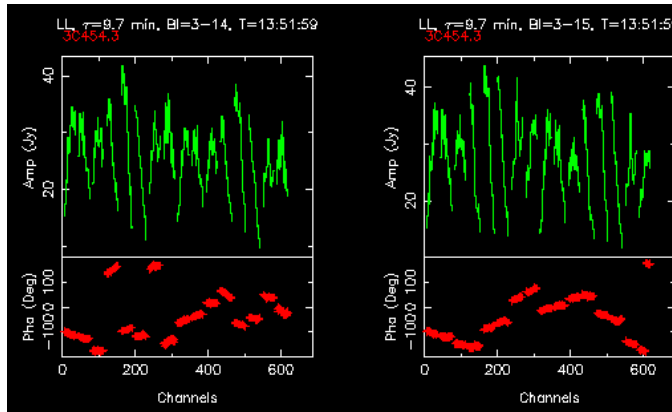


Figure 3.7: Raw spectra for passband calibrator 3C454.3. Both phases (down) and amplitudes (up) are plotted against the channels, every spectral window is separated by a space.

Passband Calibration

At this point, before the proper calibration process starts, the last thing to check is the raw spectra of the passband calibrator; here is important to check if there are spectral windows with poor signal-to-noise ratios and/or channels with bad values. The raw spectra are always displayed, for each baseline, with both amplitudes and phases on the y axis, and the channel number on the x axis (Fig 3.7). I never encountered problems in this step.

After this quick look, I found the correction coefficients by using *mfcald*, a MIRIAD task which determines calibration corrections (antenna gains, delay terms and passband responses) from a multi-frequency dataset. An example can be seen in Fig 3.8. It is easy now to apply the coefficients to the raw spectra of the calibrator, this operation should flatten the amplitudes and the phases, making them more similar to the theoretical spectra of the calibrator (Fig 3.9). However this is not always the case, and some amplitude “spikes” or “jumps” can occur, or even an unusually high dispersion in the phases (usually happening together), as seen in Fig 3.10. In cases like Fig 3.10 I had to remove the spectral windows in which the jumps occurred from the data.

The passband calibration is then applied to the gain calibrator, and usually the problems are transmitted as well. In Fig 3.11 we can see that for the same baseline 6-14 the phase distribution that should be flat is now spread. After the flagging of the “bad” spectral windows, I had to check if those errors in the spectra of the gain calibrator were corrected or not, and if not I flagged as bad that baseline for the whole track.

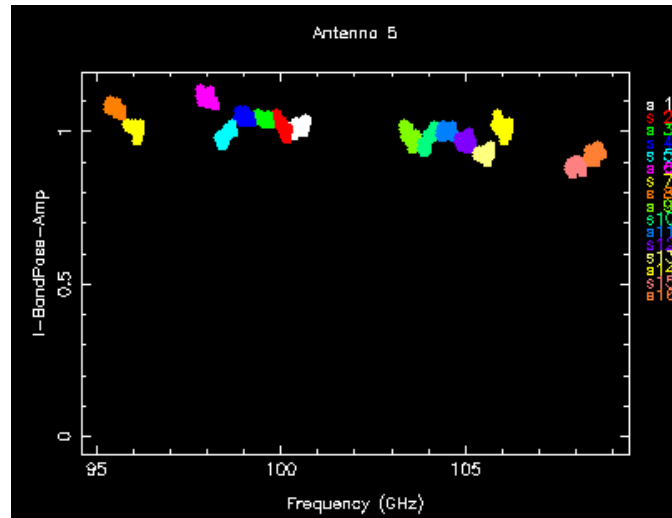


Figure 3.8: Passband calibration amplitude correction coefficients. From track c1219.1C_100Serpens.15. The different colors are for each different spectral window, like shown in the upper right corner.

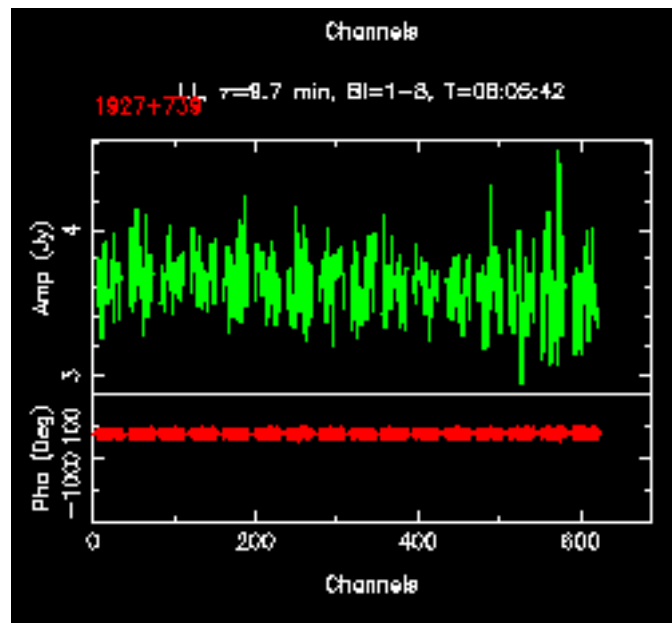


Figure 3.9: Passband calibrator 1927+739 after passband calibration. As in fig. 3.7 this plot shows both amplitudes and phases vs each spectral channel with a separation between different spectral windows. After the calibration the amplitudes and phases are more flat.

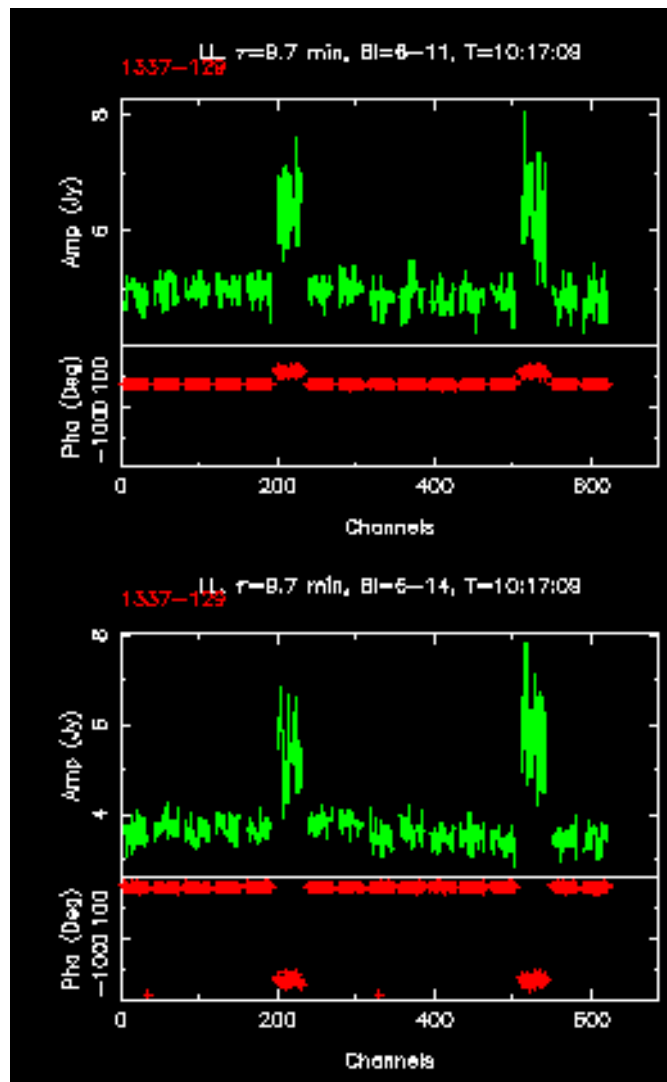


Figure 3.10: Phase and amplitude jumps after bandpass calibration in the sixth and fourteenth window.

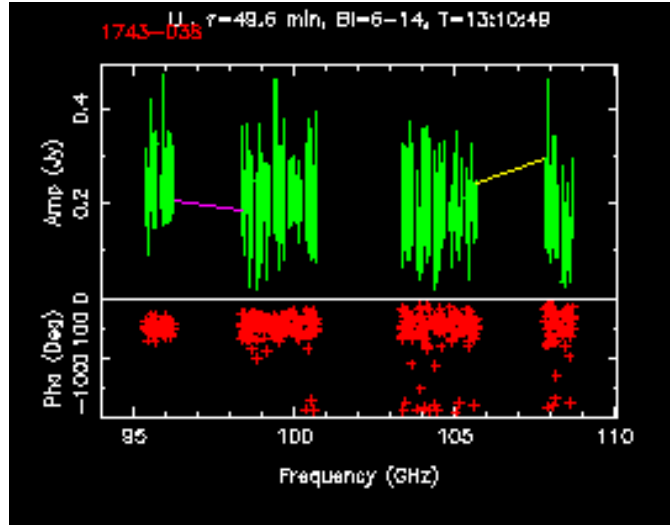


Figure 3.11: The passband calibration errors are transmitted to the gain calibrator, the 6-16 baseline is the same of the bottom plot of fig. 3.10.

Flux calibration

Like for the passband calibrator also the flux calibrator, in the tracks I analyzed, was observed only at the beginning of each track. In the tracks I analyzed, two different cases for the flux calibrators were present: whether they were resolved or unresolved. MWC349 is an example of the first case (Fig 3.12), here the amplitudes are almost the same even when measured by the longest baselines, i.e. all of them can be used for the flux calibration. Mars, or Neptune are examples of the second case (Fig 3.13), when the calibrator is resolved the Amplitude vs (u, v) distance plot the *sinc* function, mentioned in sect. 2.3, in this case only the points with amplitudes within the 30 % of the flux of the central peak were considered for the calibration.

The amplitudes were always plotted against the u, v distances, i.e. the length of the baseline in the u, v plane. As expected from a resolved source, in Fig 3.13, we can see the sinc function resulting from the interference; this situation was dealt with as explained in section 2.3. The flux was extracted using the *bootflux* command. This task gives, in the end, the flux of the gain calibrator in Jansky. 1743-038 was used as gain calibrator for every track. In Fig. 3.14 I show the different fluxes obtained for it in each track in its Julian date. The spread of the values gives the accuracy of the flux measures of the observations: the smaller the spread the more accurate the observations.

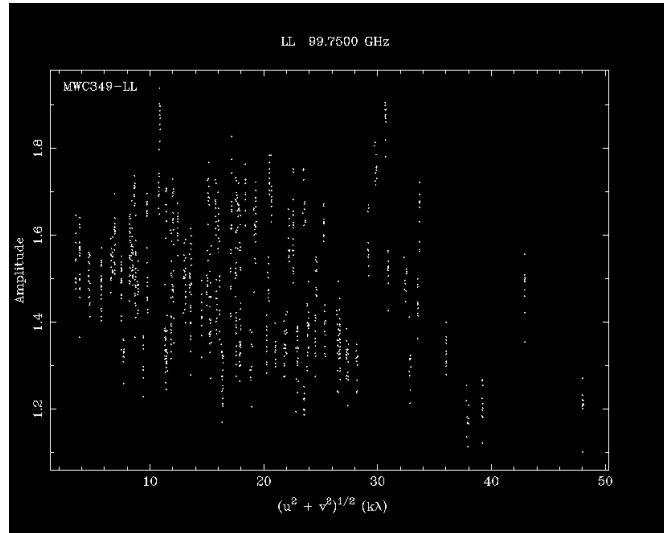


Figure 3.12: MWC349 an unresolved flux calibrator. This plot shows the measured amplitudes vs the (u, v) distances, for an unresolved calibrator this plot shows very little variations with increasing u, v distances.

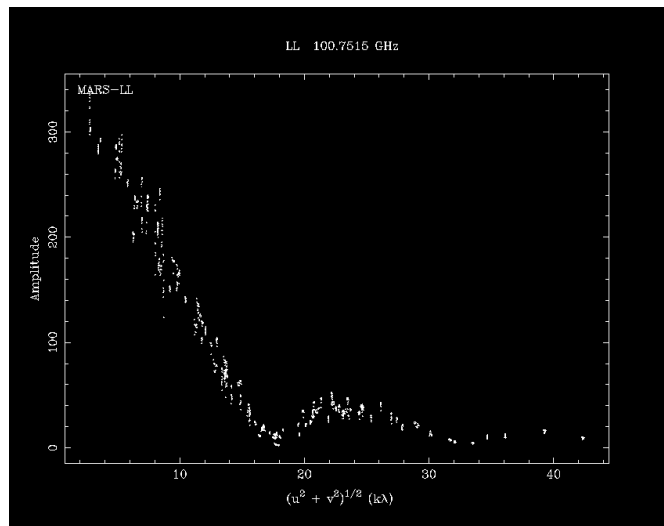


Figure 3.13: Mars, a resolved flux calibrator. This plot shows the measured amplitudes vs the (u, v) distances. For a resolved calibrator the interference *sync* function is the result of the plot.

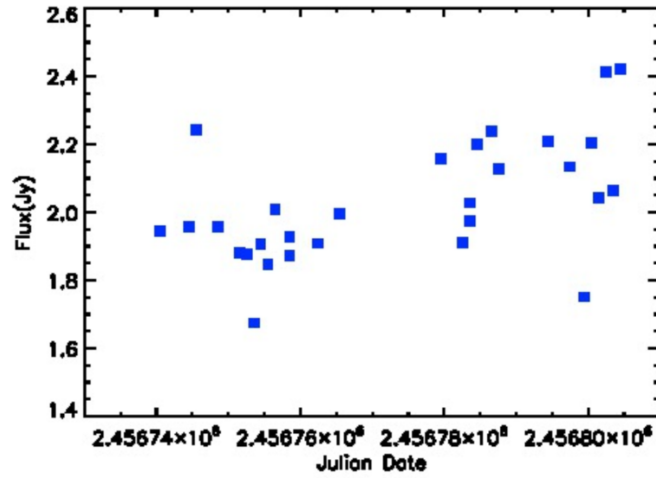


Figure 3.14: The different values of the flux for 1743-038 in each track. Some fluctuations can be seen from the plot, almost always in a 20% span. The flux of the calibrator seems higher going towards the last observations.

Gain Calibration

After the flux calibration, every amplitude and phase from each measurement of the gain calibrator can be compared with the extracted flux from the *bootflux* task and a correction coefficient, for each antenna, can be computed for both phases and amplitudes. These coefficients will also be applied, through interpolation, to the sources observed after that gain calibrator observation and before the successive one, while the passband calibration ones are applied to the entire track. In Fig 3.15 and 3.16 the results of the gain calibration process respectively for amplitudes and phases are shown. As in the previous calibration steps, even in this one, I had to pay attention to unwanted events. The unwanted events in this case were:

- All the amplitude correction coefficients for one antenna well above, or well below 1. In an ideal case they should be always 1 for every antenna. In these situations I flagged the whole data collected by that antenna.
- One point, i.e. one coefficient, well above or below the others. In this case I flagged the data starting from the last acceptable measure to the next acceptable one. If there was a clear step, between two different points in the graph, but before and after all the other were consistent, I flagged only the data taken in the time interval of in between the two observations of the gain calibrator. This is valid for both phases and amplitudes; for the amplitudes a good behavior is seen when values vary by $\sim 20\%$ or less from the ideal value of 1, while for the phases a

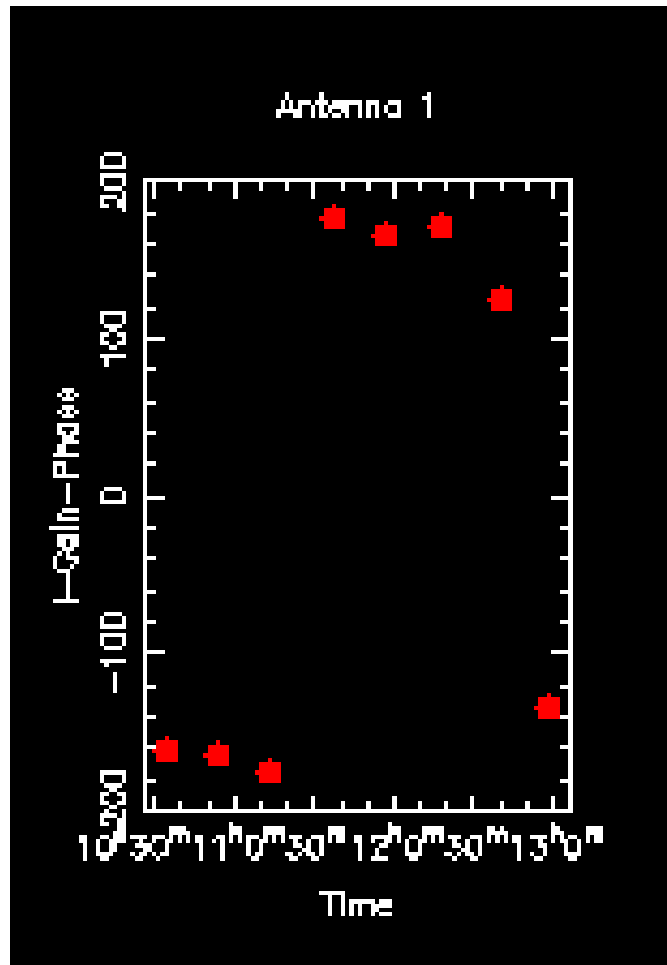


Figure 3.15: Gain calibration for phases of ant 1 from the 1D.12 track; the second last point shows jumps from the trajectory of the others and had to be removed.

good behavior is when the “track” described by the phases values are smooth and without jumps.

Figures 3.17 and 3.18 show the phase and amplitude calibration coefficients the same antenna, respectively, in the same track after the flagging process.

Amplitude and Phases vs. u,v Distance

A possible way to visualize the final product of the calibration pipeline are the graphs shown in figures 3.19 and 3.20 and their subdivisions in time for each baseline. Fig. 3.19 shows the amplitude for each observation of the gain calibrator, on the y axis, against the u,v distance, on the x axis.

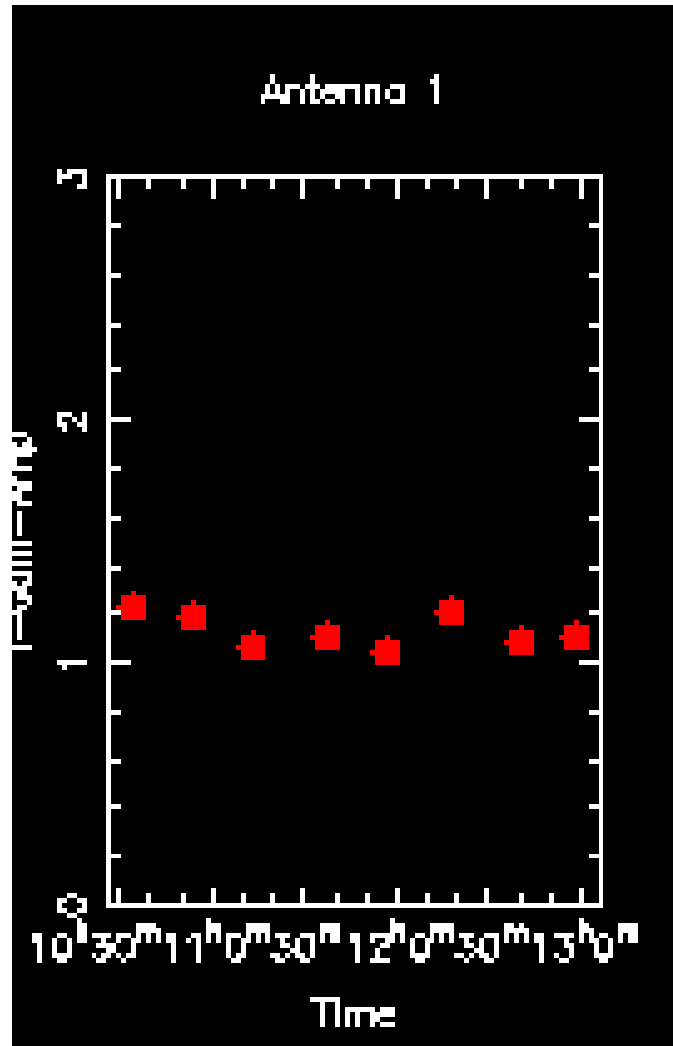


Figure 3.16: Gain calibration for the amplitudes of ant 1 from the 1D.12 track. The first two points and the third last show jumps from the others and had to be removed.

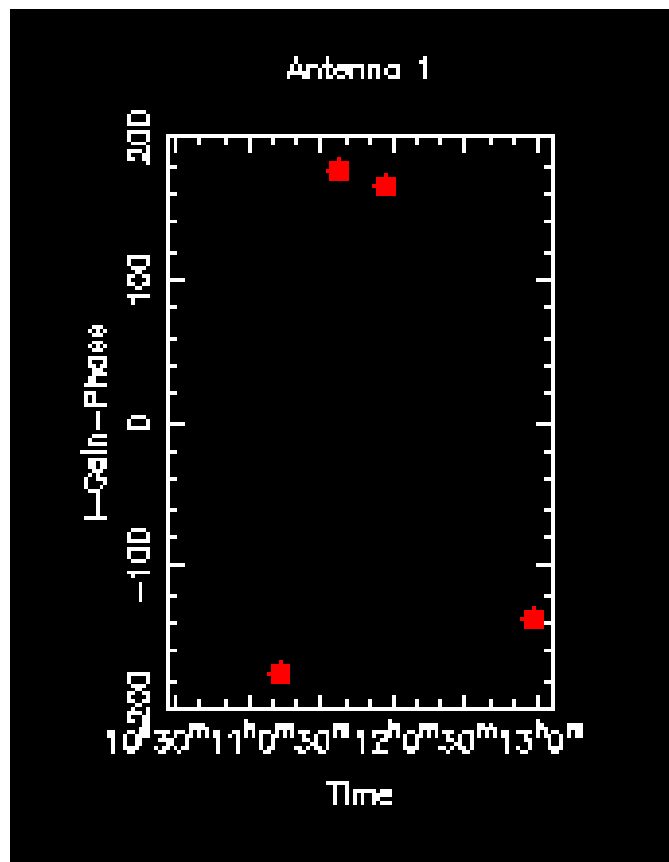


Figure 3.17: Same as fig. 3.15 but with the intervals flagged.

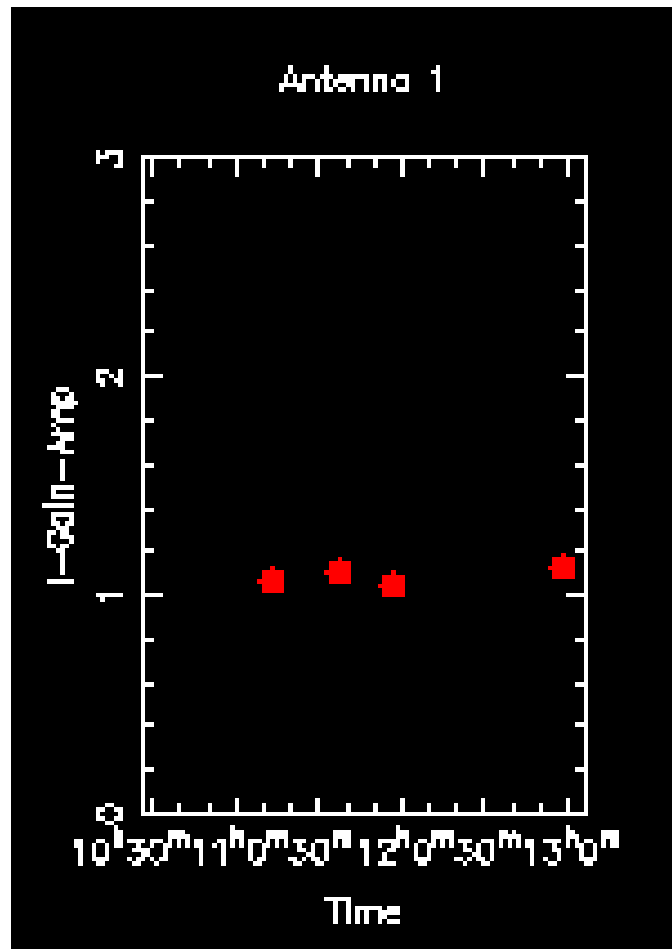


Figure 3.18: Same as fig. 3.16 but with the intervals flagged.

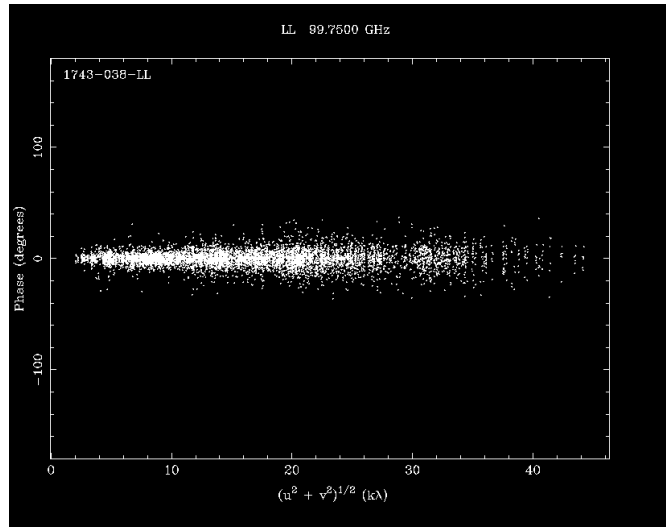


Figure 3.19: This graph, from 1D.11, shows all the phases from all the baselines sampled by the observations of the gain calibrator after the calibration.

Fig 3.20 is the same but with the phases instead of the amplitudes. From these plots I could see if some baselines still produced high, or low amplitudes or non-coherent, i.e spread out, phases and therefore proceed, as in the gain calibration step, with the flagging of the data.

Data Editing With *uvcat*

From table 3.1 it is evident that some sources were observed in different tracks. Since the aim is to produce one map for each source, I had to unite the calibrated tracks where the same source was present. This was done using the *uvcat* command. *uvcat* is a Miriad task which copies and concatenates multiple u,v dataset applying the respective calibrations while producing a single output file. This step was the end of the calibration and editing process.

3.3.3 Making the Map

After the calibration I produced the maps of each source. Even in this case I used a pre-made script called “make maps”. The script took as input files the visibility datasets produced by the calibration process and worked on them in three steps.

The first one was the plot of the dirty map. As described in sect. 2.4.1 the script, then, CLEANed this dirty map assuming that the brightest point, i.e the source, was in a square box of 10 arcsec for each side, centered on

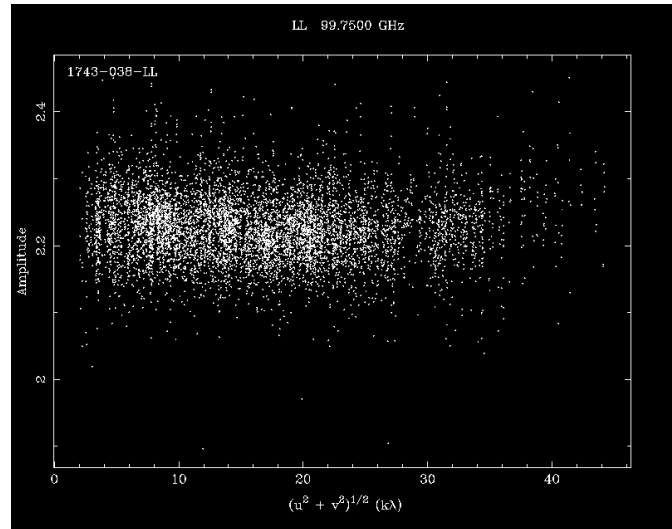


Figure 3.20: This graph, from 1D.11, shows all the amplitudes from all the baselines sampled by the observations of the gain calibrator after the calibration.

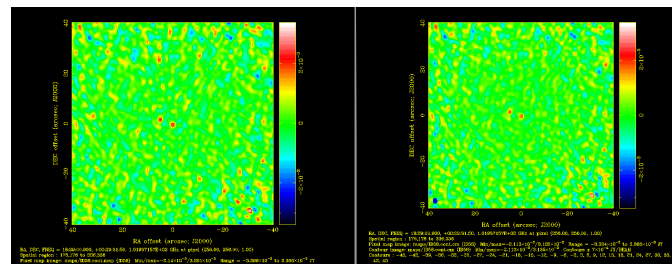


Figure 3.21: ID 58 from track 1C.7, the dirty map(left) and clean map(right)

the phase center of the observation. This was never a problem except for the ID 146 case where two other sources were detected; here to remove the artifacts of the dirty map I gave to the CLEAN algorithm 3 regions where to subtract the CLEAN components: the 3 sources. The final result is the CLEANed map. In order to use the image in CASA I created a FITS file of the clean map using the MIRIAD *fits* command. *fits* is a MIRIAD task that converts image and uv files both from FITS to MIRIAD format and vice versa.

3.3.4 Photometry with Casaviewer

After having obtained the CLEANed maps I extracted from each the root mean square (RMS), i.e. the “noise ” of the image, and the flux of the detected sources using the software CASA and its function VIEWER.

I opened the FITS files in the VIEWER, with the raster image option, selected an area around the center of the image, avoiding to include the hypothetical source in the middle or any other possible sources. In the selected region, I calculated the RMS, then I repeated this procedure modifying the shape of the selection observing the variations to the RMS value. As a final estimate of the noise I took the most representative between the ones I obtained. To generate a contour map, I opened the contour image from the same FITS file and put the value I found for the RMS in the “basic contour level ” field.

The fluxes were calculated with the same method of the RMS but, instead of selecting an empty space, I drew the limit at the “basic contour level ”, i.e. the 1σ line, and then I looked at the “maximum” and “fluxdensity ” values. If these two values were similar and $\geq 3\sigma$, and the coordinates of the source were compatible with the known coordinates of the detected disk, then, I considered it as a detection. Out of the 81 observed disks ID 3, 7, 58, 60 and 146 were detected.

For a more precise estimate of the flux of the detected sources I used the *wfit* MIRIAD command to extract the fluxes, and the RMSs, from the images by fitting a point-like source on the (u, v) plane. In table 3.2 I present the final result with all the RMSs and fluxes for all the 81 sources; where there was no detection only an upper limit to the flux could be found, hence the “ \leq ” symbol. All the upper limits are at the 3σ value.

Disk ID	RMS(mJy/beam)	Flux Density(mJy)
ID1	0.25	≤ 0.75
ID3	0.64	3.09
ID6	0.24	≤ 0.72
ID7	0.38	1.69
ID9	0.57	≤ 1.71
ID10	0.43	≤ 1.29

ID13	0.71	≤ 2.13
ID14	0.31	≤ 0.93
ID15	0.80	≤ 2.40
ID20	0.25	≤ 0.75
ID21	1.27	≤ 3.81
ID24	0.34	≤ 1.02
ID29	0.31	≤ 0.93
ID30	0.38	≤ 1.14
ID32	0.28	≤ 0.84
ID36	0.25	≤ 0.75
ID38	0.24	≤ 0.72
ID40	0.54	≤ 1.62
ID41	0.42	≤ 1.26
ID43	0.35	≤ 1.05
ID48	1.50	≤ 4.50
ID52	0.46	≤ 1.38
ID53	1.11	≤ 3.33
ID54	0.30	≤ 0.90
ID55	0.40	≤ 1.20
ID58	0.33	2.34
ID59	0.33	≤ 0.99
ID60	0.39	1.77
ID61	0.51	≤ 1.53
ID62	0.80	≤ 2.40
ID64	0.92	≤ 2.76
ID65	0.27	≤ 0.81
ID66	0.30	≤ 0.90
ID69	0.26	≤ 0.78
ID70	0.43	≤ 1.29
ID71	0.27	≤ 0.81
ID75	0.34	≤ 1.12
ID76	0.28	≤ 0.81
ID80	0.35	≤ 1.05
ID81	0.32	≤ 0.96
ID82	0.30	≤ 0.90
ID83	0.31	≤ 0.93
ID86	0.35	≤ 1.05
ID87	0.31	≤ 0.93
ID88	0.28	≤ 0.84
ID89	0.31	≤ 0.93
ID90	0.35	≤ 1.05

ID92	0.34	≤ 1.02
ID96	0.50	≤ 1.50
ID97	0.39	≤ 1.17
ID98	0.49	≤ 1.47
ID100	0.46	≤ 1.38
ID103	0.33	≤ 0.99
ID104	0.41	≤ 1.23
ID105	0.48	≤ 1.44
ID106	0.49	≤ 1.47
ID109	0.97	≤ 2.91
ID111	0.29	≤ 0.87
ID113	0.40	≤ 1.20
ID114	0.39	≤ 1.17
ID115	0.51	≤ 1.53
ID116	0.31	≤ 0.93
ID119	0.30	≤ 0.90
ID120	0.39	≤ 1.17
ID122	0.55	≤ 1.65
ID123	0.35	≤ 1.05
ID124	0.54	≤ 1.62
ID125	0.34	≤ 1.02
ID127	0.36	≤ 1.08
ID129	0.49	≤ 1.47
ID130	0.47	≤ 1.41
ID131	0.36	≤ 1.08
ID136	0.33	≤ 0.99
ID137	0.70	≤ 2.10
ID139	0.29	≤ 0.87
ID142	0.38	≤ 1.14
ID145	0.33	≤ 0.99
ID146	0.54	17.99
ID147	0.38	≤ 1.14
ID148	0.50	≤ 1.50
ID149	0.30	≤ 0.90

Table 3.3: Table showing the RMSs and fluxes of all the sources in the survey.

Chapter 4

Results

In the first section of this chapter I will present the derivation of the dust masses for the 81 YSOs. In the second section I will illustrate the conclusions that can be inferred from the results of the analysis. In the third, and last, section I will briefly resume all the work I did and I will explain some possible future perspectives for this project.

4.1 Data Analysis

Recalling eq. 1.23 it is possible to retrieve the dust masses from the measured fluxes listed in table 3.2 using:

$$M_{dust} = \frac{d^2 F}{\kappa_{mm}^i B_{mm}}, \quad (4.1)$$

where B_{mm} was calculated at with $T = 20\text{K}$, $d = 415\text{pc}$ and $k_{mm}^i = 1\text{cm}^2\text{g}^{-1}$ following the law by Beckwith (1990).

The results are shown in tab 4.1 together with other properties for the disk and stars from Oliveira (2013).

Disk	M_{dust} (M_{\oplus})	ST	T_{eff} (K)	L_{star} L_{\odot}	L_{disk} L_{\odot}	Age (Myr)	Mass (M_{\odot})
ID1	≤ 3.35	K2	4900^{+610}_{-450}	$1.07^{+0.88}_{-0.50}$	$0.13^{+0.14}_{-0.14}$	$10.86^{+16.99}_{-7.04}$	$1.27^{+0.31}_{-0.31}$
ID3	$13.80^{+2.85}_{-2.85}$	M0	3850^{+120}_{-80}	$1.77^{+1.55}_{-0.84}$	$0.53^{+0.94}_{-0.50}$	$0.50^{+1.40}_{-0.50}$	$1.04^{+0.18}_{-0.10}$
ID6	≤ 3.22	K5	4350^{+330}_{-340}	$3.30^{+1.79}_{-1.17}$	$0.27^{+0.89}_{-0.89}$	$2.37^{+0.30}_{-0.30}$	$1.48^{+0.27}_{-0.27}$
ID7	$7.54^{+1.69}_{-1.69}$	M0	3850^{+120}_{-80}	$0.51^{+2.36}_{-0.42}$	$1.56^{+0.80}_{-0.80}$	$4.36^{+47.42}_{-4.36}$	$0.88^{+0.28}_{-0.24}$
ID9	≤ 7.64	M0	3850^{+190}_{-220}	$3.23^{+2.82}_{-1.53}$	$0.38^{+1.22}_{-1.22}$	$0.56^{+0.56}_{-0.56}$	$1.03^{+1.03}_{-1.03}$
ID10	≤ 5.76	M3	3470^{+220}_{-260}	$1.82^{+1.59}_{-0.87}$	$0.18^{+0.32}_{-0.32}$	$0.44^{+0.44}_{-0.44}$	$0.68^{+0.68}_{-0.68}$
ID13	≤ 9.51	M7	2940^{+340}_{-390}	$0.12^{+0.10}_{-0.06}$	$0.15^{+0.02}_{-0.02}$	$2.54^{+2.54}_{-2.54}$	$0.24^{+0.24}_{-0.24}$
ID14	≤ 4.15	M2	3580^{+250}_{-230}	$0.49^{+0.43}_{-0.23}$	—	$2.27^{+3.45}_{-1.50}$	$0.63^{+0.28}_{-0.19}$
ID15	≤ 10.72	M0	3850^{+190}_{-220}	$1.32^{+1.15}_{-0.63}$	$0.49^{+0.64}_{-0.64}$	$1.01^{+1.74}_{-1.01}$	$0.98^{+0.16}_{-0.18}$
ID20	≤ 3.35	M0	3850^{+190}_{-220}	$0.29^{+0.25}_{-0.14}$	$0.05^{+0.01}_{-0.00}$	$9.06^{+14.45}_{-5.16}$	$0.81^{+0.08}_{-0.25}$
ID21	≤ 17.02	M0	3850^{+190}_{-220}	$0.66^{+0.58}_{-0.32}$	$0.15^{+0.10}_{-0.10}$	$2.89^{+4.58}_{-1.74}$	$0.91^{+0.14}_{-0.26}$
ID24	≤ 4.56	M7	2940^{+340}_{-290}	$0.15^{+0.13}_{-0.07}$	$0.14^{+0.02}_{-0.02}$	$2.06^{+20.6}_{-2.06}$	$0.24^{+0.24}_{-0.24}$
ID29	≤ 4.15	M2	3580^{+320}_{-360}	$0.18^{+0.16}_{-0.09}$	$0.20^{+0.04}_{-0.04}$	$8.13^{+18.42}_{-6.50}$	$0.56^{+0.23}_{-0.32}$
ID30	≤ 5.09	M1	3720^{+150}_{-120}	$1.00^{+0.53}_{-0.36}$	$0.10^{+0.10}_{-0.10}$	$1.18^{+1.13}_{-0.74}$	$0.83^{+0.18}_{-0.10}$
ID32	≤ 3.75	M6	3050^{+370}_{-360}	$0.30^{+0.25}_{-0.14}$	$0.22^{+0.06}_{-0.06}$	$1.73^{+1.73}_{-1.73}$	$0.38^{+0.38}_{-0.38}$
ID36	≤ 3.35	K5	4350^{+680}_{-480}	$2.88^{+1.56}_{-1.02}$	$0.50^{+1.43}_{-1.43}$	$1.20^{+4.56}_{-1.20}$	$1.21^{+0.50}_{-0.66}$

ID38	≤ 3.22	K7	4060 ⁺³⁵⁰ ₋₈₀	0.18 ^{+0.16} _{-0.09}	0.02 ^{+0.00} _{-0.00}	21.77 ^{+39.11} _{-13.85}	0.72 ^{+0.02} _{-0.11}
ID40	≤ 7.24	M7	2940 ⁺⁵⁷⁰ ₋₅₀₇	0.36 ^{+0.30} _{-0.17}	4.46 ^{+1.61} _{-1.61}	2.03 ^{+2.03} _{-2.03}	0.48 ^{+0.48} _{-0.48}
ID41	≤ 5.63	K2	4900 ⁺⁶¹⁰ ₋₄₅₀	0.11 ^{+0.09} _{-0.05}	0.28 ^{+0.03} _{-0.03}	-	-
ID43	≤ 4.69	M0.5	3785 ⁺²²⁵ ₋₃₈₀	0.18 ^{+0.16} _{-0.09}	0.56 ^{+0.10} _{-0.10}	18.20 ^{+25.92} _{-15.10}	0.75 ^{+0.08} _{-0.37}
ID48	≤ 20.10	M5.5	3145 ⁺⁴²⁵ ₋₅₂₅	0.34 ^{+0.29} _{-0.16}	1.32 ^{+0.44} _{-0.44}	1.58 ^{+1.07} _{-1.07}	0.33 ^{+0.19} _{-0.19}
ID52	≤ 6.16	G3	5830 ⁺⁴⁰⁰ ₋₂₃₀	8.14 ^{+6.40} _{-4.07}	0.05 ^{+0.43} _{-0.43}	6.93 ^{+6.33} _{-2.63}	1.82 ^{+0.38} _{-0.38}
ID53	≤ 14.88	M2.5	3525 ⁺³⁸⁵ ₋₃₅₅	0.35 ^{+0.31} _{-0.17}	0.06 ^{+0.02} _{-0.02}	2.34 ^{+6.84} _{-2.34}	0.50 ^{+0.41} _{-0.36}
ID54	≤ 4.02	M0	3850 ⁺¹⁹⁰ ₋₂₂₀	0.58 ^{+0.51} _{-0.28}	1.61 ^{+0.94} _{-0.94}	3.44 ^{+5.18} _{-1.97}	0.90 ^{+0.14} _{-0.26}
ID55	≤ 5.35	K2	4900 ⁺⁴⁵⁰ ₋₂₁₀	2.44 ^{+10.94} _{-2.03}	0.04 ^{+0.09} _{-0.09}	4.02 ^{+36.50} _{-4.02}	1.68 ^{+1.13} _{-0.80}
ID58	10.45 ^{+1.47} _{-1.47}	K7	4060 ⁺³⁵⁰ ₋₈₀	1.19 ^{+5.48} _{-0.98}	3.89 ^{+4.62} _{-4.62}	2.31 ^{+24.92} _{-2.31}	1.14 ^{+0.25} _{-0.14}
ID59	≤ 4.42	M0	3850 ⁺¹⁹⁰ ₋₂₂₀	0.51 ^{+0.44} _{-0.24}	2.94 ^{+1.49} _{-1.49}	4.42 ^{+5.41} _{-2.58}	0.87 ^{+0.14} _{-0.26}
ID60	7.90 ^{+1.74} _{-1.74}	M0.5	3785 ⁺⁵⁰ ₋₈₀	0.83 ^{+0.73} _{-0.40}	1.17 ^{+0.97} _{-0.97}	2.20 ^{+3.35} _{+1.51}	0.93 ^{+0.08} _{-0.10}
ID61	≤ 6.83	M0	3850 ⁺¹²⁰ ₋₈₀	3.65 ^{+1.19} _{-1.73}	0.24 ^{+0.87} _{-0.87}	0.40 ^{+0.40} _{-0.40}	1.05 ^{+1.05} _{-1.05}
ID62	≤ 10.72	K0	5250 ⁺⁶³⁰ ₋₁₁₄₀	18.94 ^{+15.34} _{-9.34}	0.33 ^{+6.16} _{-6.16}	-	-
ID64	≤ 12.33	M5	3240 ⁺²⁷⁰ ₋₂₆₀	0.13 ^{+0.11} _{-0.06}	0.58 ^{+0.08} _{-0.08}	2.05 ^{+5.19} _{-2.05}	0.21 ^{+0.21} _{-0.11}
ID65	≤ 3.62	M6	3050 ⁺³⁷⁰ ₋₃₆₀	0.20 ^{+0.17} _{-0.10}	2.46 ^{+0.49} _{-0.49}	1.48 ^{+1.11} _{-1.11}	0.23 ^{+0.12} _{-0.12}
ID66	≤ 4.02	K5	4350 ⁺³³⁰ ₋₃₄₀	5.11 ^{+4.35} _{-2.46}	0.39 ^{+1.99} _{-1.99}	1.64 ^{+0.17} _{-0.17}	1.56 ^{+0.35} _{-0.35}
ID69	≤ 3.48	M5	3240 ⁺²⁷⁰ ₋₂₆₀	0.23 ^{+0.20} _{-0.11}	0.00 ^{+0.00} _{-0.00}	0.77 ^{+0.22} _{-0.22}	0.21 ^{+0.23} _{-0.07}
ID70	≤ 5.76	A3	8720 ⁺⁷²⁰ ₋₇₇₅	20.64 ^{+15.11} _{-10.63}	0.01 ^{+0.22} _{-0.22}	8.18 ^{+70.19} _{-8.18}	2.10 ^{+0.38} _{-0.21}
ID71	≤ 3.62	M3	3470 ⁺⁸⁰ ₋₁₃₀	0.33 ^{+0.29} _{-0.16}	0.03 ^{+0.01} _{-0.01}	2.48 ^{+3.15} _{-1.37}	0.49 ^{+0.09} _{-0.11}
ID75	≤ 5.00	M5	3240 ⁺²⁷⁰ ₋₂₇₀	0.11 ^{+0.10} _{-0.05}	0.23 ^{+0.03} _{-0.03}	2.33 ^{+5.95} _{-2.33}	0.21 ^{+0.21} _{-0.11}
ID76	≤ 3.62	M1	3720 ⁺¹⁵⁰ ₋₁₂₀	0.33 ^{+0.29} _{-0.16}	0.11 ^{+0.04} _{-0.04}	5.66 ^{+7.09} _{-3.29}	0.71 ^{+0.16} _{-0.14}
ID80	≤ 4.69	F0	7200 ⁺³⁸⁰ ₋₃₁₀	370.90 ^{+288.34} _{-86.29}	0.17 ^{+62.16} _{-62.16}	-	-
ID81	≤ 4.29	M5	3240 ⁺⁵²⁰ ₋₆₉₀	60.77 ^{+52.31} _{-29.09}	0.12 ^{+7.38} _{-7.38}	-	-
ID82	≤ 4.02	M0	3850 ⁺¹⁹⁰ ₋₂₂₀	0.20 ^{+0.10} _{-0.10}	0.03 ^{+0.01} _{-0.01}	15.80 ^{+21.23} _{-9.13}	0.76 ^{+0.08} _{-0.22}
ID83	≤ 4.14	M6	3050 ⁺³⁷⁰ ₋₃₆₀	0.31 ^{+0.26} _{-0.15}	0.04 ^{+0.01} _{-0.01}	1.64 ^{+1.64} _{-1.64}	0.38 ^{+0.38} _{-0.38}
ID86	≤ 4.69	M5.5	3145 ⁺²⁷⁰ ₋₁₇₀	35.78 ^{+30.57} _{-17.19}	0.15 ^{+5.50} _{-5.50}	-	-
ID87	≤ 4.15	M4	3370 ⁺³²⁰ ₋₄₆₀	0.82 ^{+0.72} _{-0.39}	0.34 ^{+0.28} _{-0.28}	1.43 ^{+0.24} _{-0.24}	0.64 ^{+0.19} _{-0.19}
ID88	≤ 3.75	M0.5	3785 ⁺¹⁵⁵ ₋₂₇₅	0.64 ^{+0.56} _{-0.31}	1.04 ^{+0.67} _{-0.67}	2.98 ^{+4.76} _{-4.76}	0.91 ^{+0.12} _{-0.30}
ID89	≤ 4.15	K5	4350 ⁺⁸⁵⁰ ₋₅₅₀	0.95 ^{+0.81} _{-0.46}	0.21 ^{+0.20} _{-0.20}	5.11 ^{+21.66} _{-3.76}	1.18 ^{+0.02} _{-0.62}
ID90	≤ 4.69	M7	2940 ⁺⁶⁸⁰ ₋₅₀₇	0.19 ^{+0.16} _{-0.09}	0.40 ^{+0.08} _{-0.08}	7.34 ^{+7.34} _{-7.34}	0.54 ^{+0.54} _{-0.54}
ID92	≤ 4.56	M0	3850 ⁺¹²⁰ ₋₈₀	0.58 ^{+0.51} _{-0.28}	0.39 ^{+0.23} _{-0.23}	3.40 ^{+5.17} _{-1.95}	0.90 ^{+0.10} _{-0.10}
ID96	≤ 6.70	M1	3720 ⁺¹⁵⁰ ₋₁₂₀	0.34 ^{+0.30} _{-0.16}	0.16 ^{+0.06} _{-0.06}	5.51 ^{+6.80} _{-3.19}	0.72 ^{+0.16} _{-0.14}
ID97	≤ 5.23	M2	3580 ⁺²⁵⁰ ₋₂₃₀	0.14 ^{+0.08} _{-0.05}	0.14 ^{+0.02} _{-0.02}	10.11 ^{+18.68} _{-6.67}	0.55 ^{+0.19} _{-0.22}
ID98	≤ 6.57	A3	8270 ⁺³¹⁰⁰ ₋₁₂₂₀	32.48 ^{+23.78} _{-16.72}	0.00 ^{+0.12} _{-0.12}	4.99 ^{+7.78} _{-1.68}	2.42 ^{+0.45} _{-0.44}
ID100	≤ 6.16	M6	3050 ⁺³⁷⁰ ₋₃₆₀	0.18 ^{+0.15} _{-0.09}	0.24 ^{+0.04} _{-0.04}	1.61 ^{+1.15} _{-1.15}	0.22 ^{+0.12} _{-0.12}
ID103	≤ 4.43	M6	3050 ⁺³⁷⁰ ₋₂₆₀	166.68 ^{+141.01} _{-80.49}	0.06 ^{+0.69} _{-0.69}	-	-
ID104	≤ 5.49	M5	3240 ⁺²⁷⁰ ₋₂₆₀	0.12 ^{+0.11} _{-0.06}	0.10 ^{+0.01} _{-0.01}	2.16 ^{+5.49} _{-2.16}	0.21 ^{+0.21} _{-0.11}
ID105	≤ 6.43	M5	3240 ⁺²⁷⁰ ₋₂₆₀	0.09 ^{+0.05} _{-0.03}	0.00 ^{+0.00} _{-0.00}	2.91 ^{+7.96} _{-2.91}	0.21 ^{+0.20} _{-0.12}
ID106	≤ 6.57	M3	3470 ⁺⁸⁰ ₋₁₃₀	0.25 ^{+0.13} _{-0.09}	0.02 ^{+0.01} _{-0.01}	3.10 ^{+3.20} _{-1.02}	0.47 ^{+0.08} _{-0.11}
ID109	≤ 12.99	M7	3940 ⁺³⁴⁰ ₋₃₉₀	0.22 ^{+0.19} _{-0.11}	0.19 ^{+0.04} _{-0.04}	1.16 ^{+0.16} _{-1.16}	0.25 ^{+0.25} _{-0.25}
ID111	≤ 3.89	M5	3240 ⁺²⁷⁰ ₋₂₆₀	0.07 ^{+0.04} _{-0.02}	0.11 ^{+0.01} _{-0.01}	4.26 ^{+13.41} _{-0.26}	0.20 ^{+0.20} _{-0.11}
ID113	≤ 5.36	K7	4060 ⁺³⁵⁰ ₋₈₀	2.32 ^{+2.02} _{-1.11}	0.03 ^{+0.08} _{-0.08}	0.68 ^{+1.66} _{-0.13}	0.13 ^{+0.91} _{-0.22}
ID114	≤ 5.23	F9	6115 ⁺³⁹⁰ ₋₄₀₀	3.68 ^{+2.87} _{-1.84}	0.07 ^{+0.24} _{-0.24}	14.29 ^{+17.38} _{-14.15}	116.38 ^{+1.39} _{-0.18}
ID115	≤ 6.83	M0.5	3785 ⁺¹⁵⁵ ₋₂₇₅	0.50 ^{+0.43} _{-0.24}	0.17 ^{+0.09} _{-0.09}	4.58 ^{+5.47} _{-2.84}	0.87 ^{+0.12} _{-0.31}
ID116	≤ 4.15	M5	3240 ⁺²⁷⁰ ₋₂₆₀	0.21 ^{+0.18} _{-0.10}	0.05 ^{+0.01} _{-0.01}	0.93 ^{+2.29} _{-0.93}	0.21 ^{+0.22} _{-0.08}
ID119	≤ 4.02	K7	4060 ⁺³⁵⁰ ₋₈₀	0.46 ^{+0.40} _{-0.22}	0.02 ^{+0.01} _{-0.01}	4.86 ^{+9.08} _{-2.33}	0.73 ^{+0.27} _{-0.09}
ID120	≤ 5.23	A2	8970 ⁺⁵²⁰ ₋₅₄₀	25.13 ^{+18.67} _{-12.86}	0.00 ^{+0.06} _{-0.06}	6.69 ^{+2.10} _{-6.69}	2.24 ^{+0.35} _{-0.29}
ID122	≤ 7.37	M0	3850 ⁺¹⁵⁵ ₋₁₂₀	1.10 ^{+0.96} _{-0.53}	0.03 ^{+0.03} _{-0.03}	1.43 ^{+2.03} _{-1.12}	0.96 ^{+0.15} _{-0.16}
ID123	≤ 4.69	M0	3850 ⁺¹²⁰ ₋₈₀	0.72 ^{+0.63} _{-0.34}	0.12 ^{+0.09} _{-0.09}	2.63 ^{+4.10} _{-1.66}	0.92 ^{+0.12} _{-0.10}
ID124	≤ 7.24	M0	3850 ⁺¹⁵⁵ ₋₁₅₀	0.27 ^{+0.15} _{-0.10}	0.08 ^{+0.02} _{-0.02}	9.68 ^{+10.12} _{-3.71}	0.81 ^{+0.06} _{-0.17}
ID125	≤ 4.56	M0	3850 ⁺¹²⁰ ₋₈₀	0.58 ^{+0.51} _{-0.28}	0.07 ^{+0.04} _{-0.04}	3.45 ^{+5.18} _{-1.98}	0.90 ^{+0.10} _{-0.10}
ID127	≤ 4.82	M2	3580 ⁺¹²⁰ ₋₁₃₀	0.48 ^{+0.42} _{-0.23}	0.03 ^{+0.02} _{-0.02}	2.35 ^{+3.15} _{-1.46}	0.63 ^{+0.12} _{-0.12}
ID129	≤ 6.57	M7	2940 ⁺³⁴⁰ ₋₃₉₀	0.22 ^{+0.18} _{-0.11}	1.32 ^{+0.29} _{-0.29}	1.23 ^{+1.23} _{-1.23}	0.25 ^{+0.25} _{-0.25}
ID130	≤ 6.30	K6	4205 ⁺¹⁴⁰ ₋₁₅₀	1.33 ^{+0.64} _{-0.64}	0.22 ^{+0.30} _{-0.30}	2.16 ^{+2.43} _{-2.16}	0.91 ^{+0.16} _{-0.16}
ID131	≤ 4.82	A3	8720 ⁺⁷²⁰ ₋₇₇₅	25.57 ^{+18.72} _{-13.16}	0.00 ^{+0.02} _{-0.02}	6.49 ^{+2.08} _{-6.49}	2.23 ^{+0.37} _{-0.30}
ID136	≤ 4.42	M5	3240 ⁺²⁷⁰ ₋₂₆₀	0.17 ^{+0.09} _{-0.06}	0.04 ^{+0.01} _{-0.01}	1.44 ^{+3.61} _{-1.44}	0.21 ^{+0.22} _{-0.10}
ID137	≤ 9.38	M2	3580 ⁺²⁵⁰ ₋₂₃₀	1.56 ^{+1.36} _{-0.74}	0.31 ^{+0.48} _{-0.48}	1.01 ^{+0.06} _{-0.06}	0.89 ^{+0.18} _{-0.18}
ID139	≤ 3.89	A4	8460 ⁺¹¹²⁰ ₋₈₂₀	33.71 ^{+24.87} _{-17.30}	0.00 ^{+0.15} _{-0.15}	4.77 ^{+4.60} _{-1.79}	2.43 ^{+0.39} _{-0.45}
ID142	≤ 5.09	M4	3370 ⁺¹⁸⁰ ₋₁₅₀	0.17 ^{+0.09} _{-0.06}	0.26 ^{+0.05} _{-0.05}	3.05 ^{+4.84} _{-3.05}	0.36 ^{+0.18} _{-0.23}
ID145	≤ 4.42	G2.5	5845 ⁺²³⁰ ₋₃₀	19.73 ^{+15.51} _{-9.86}	0.05 ^{+1.01} _{-1.01}	3.19 ^{+2.66} _{-0.89}	2.47 ^{+0.44} _{-0.52}
ID146	80.36 ^{+2.41} _{-2.41}	M4	3370 ⁺¹⁸⁰ ₋₃₅₀	0.34 ^{+0.30} _{-0.16}	89.10 ^{+30.44} _{-30.44}	1.65 ^{+1.39} _{-1.65}	0.42 ^{+0.16} _{-0.26}

ID147	≤ 5.09	M5	3240^{+270}_{-260}	$0.31^{+0.27}_{-0.15}$	$0.10^{+0.03}_{-0.03}$	$0.37^{+1.98}_{-0.37}$	$0.20^{+0.26}_{-0.05}$
ID148	≤ 6.70	K7	4060^{+350}_{-80}	$0.83^{+0.72}_{-0.40}$	$0.04^{+0.03}_{-0.03}$	$2.58^{+2.87}_{-1.48}$	$0.70^{+0.42}_{-0.08}$
ID149	≤ 4.02	M0	3850^{+190}_{-220}	$0.42^{+0.37}_{-0.20}$	$0.04^{+0.02}_{-0.02}$	$5.82^{+7.72}_{-3.47}$	$0.85^{+0.14}_{-0.26}$

Table 4.1: The obtained dust masses and the correspondent errors. The other properties are taken from Oliveira (2013). ST is the spectral type of the central star.

As it can be seen from the table, only 5 out of the 81 sources were detected: ID 3,7,58,60 and 146 (shown in the figures below), for the remaining 76 only an upper limit could be inferred. The range in dust mass, for the detected disks, spans from the ~ 7.5 Earth masses of ID 7 to the ~ 80 Earth masses of ID 146; for the remaining non detected objects the upper limits almost all $\leq 8M_{\oplus}$; spanning from the $\sim 3M_{\oplus}$ of ID 1 to the $\sim 20M_{\oplus}$ of ID 48.

It is relevant to note that for dust masses $\sim 1 - 3M_{\oplus}$, the formation of new planets is unlikely to happen. While this could be the case for some of the undetected objects, all the detected ones show dust masses superior to this limit; meaning that the planet formation process could still be happening in these disks, especially ID 146.

Finally, it is worth giving an estimate for the gas mass of the detected disks using the $M_{gas}/M_{dust} = 100$ ratio mentioned in sect. 1.3, under this assumption I obtained 4.3 Jupiter masses for ID 3, 2.3 for ID7, 3.3 for ID 58, 2.4 for ID 60 and 25.2 for ID 146. This indicates that, if the gas-to-dust mass ratio is similar to the ISM value, these five disks would still contain enough gas to form giant planets.

4.2 Relations Between Disk and Stellar Properties

Unfortunately with only five YSOs detected it is impossible to infer decisive conclusions on some possible relations between the central star and the properties of the disk, but some trend can still be investigated.

Fig. 4.5 shows the plot of the YSO age vs the dust masses I derived; from this plot it is possible to note that all the detected disks are on the younger, i.e. left, side of the axis with ages lower than 5 Myrs. Another thing that comes into sight is that no disks have been detected with ages > 5 Myr, this could imply an evolutionary process, like say planet formation or photo evaporation, that if true, makes the dust grain disappear. In fig 4.6 is shown the relation between the disk luminosity (from Oliveira 2013), in the infrared, and the dust mass I obtained. It is possible to note that the detected disks are all towards the highest disk luminosities found by Oliveira, suggesting a trend between IR luminosity, that traces dust in the disk upper layers, and sub-mm luminosity, which traces dust in the disk midplane. Probably the most interesting plot is the one in fig. 4.7 reporting the stellar

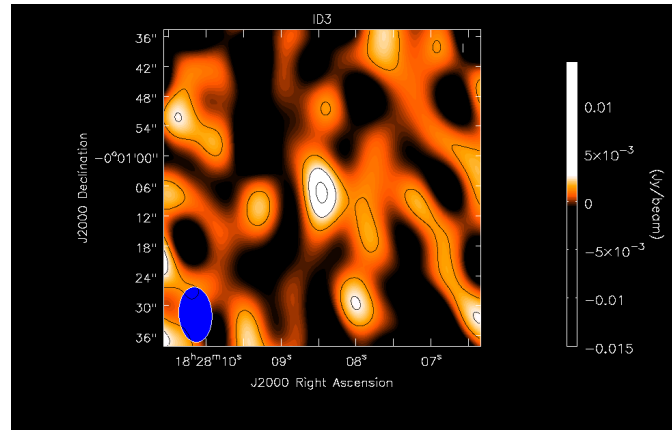


Figure 4.1: Final image of ID 3. The contours shown are respectively at 1,2 and 3 σ

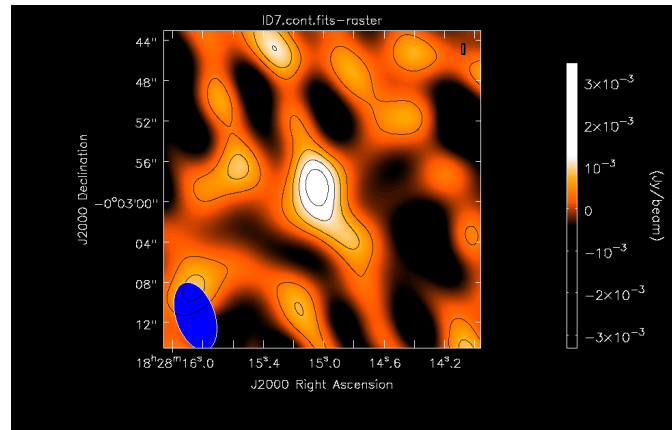


Figure 4.2: Final image of ID 7. The contours shown are respectively at 1,2,3 and 5 σ

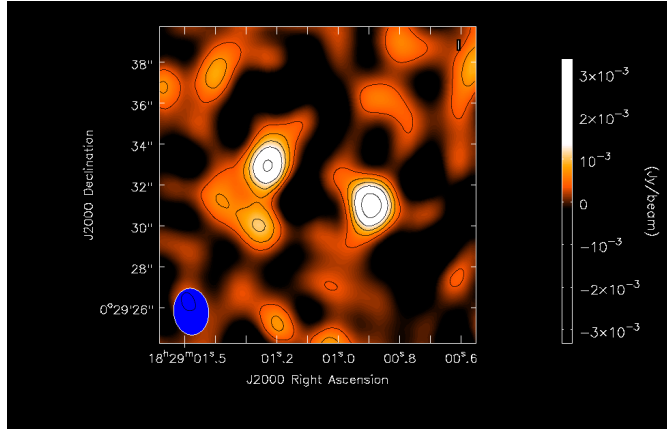


Figure 4.3: Final image comprising ID 58 (left) and ID 60 (right). The contours shown are respectively at 1,2,3,5 and 7 σ

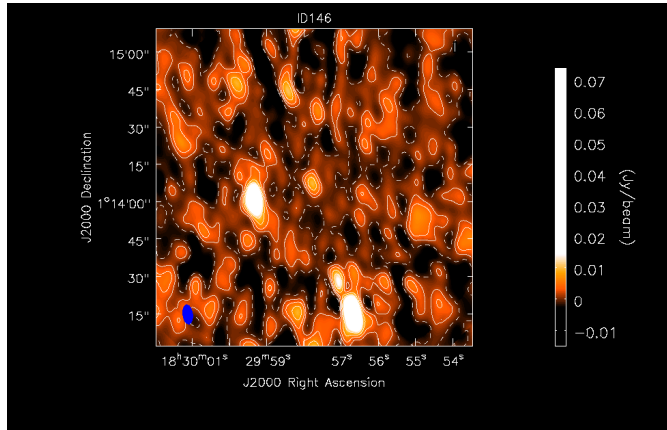


Figure 4.4: Image of ID 146 (center). On the left, of ID 146, S14 from Lee et al. (2014) was detected with a flux of 68.89 ± 2.41 mJy which is consistent with their data. On the bottom another object was detected, always using the names from Lee et. al, it is S11 and I found a flux of 93 ± 2.41 mJy which is smaller than the 106 ± 3 mJy they found, probably due to the distance from the center in our case.

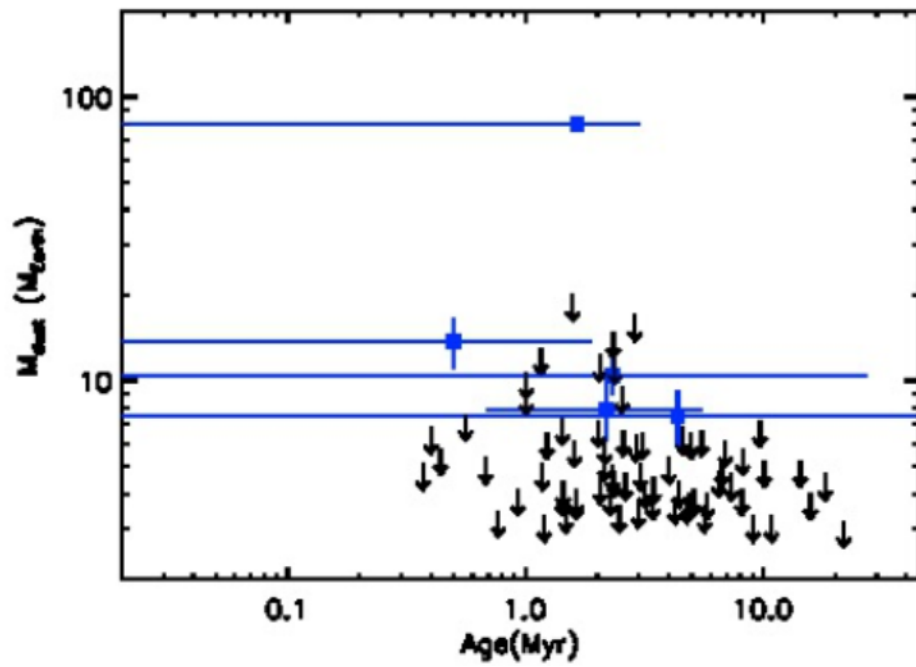


Figure 4.5: Plot showing the relation between the ages (from Oliveira, 2013) and the dust masses. The blue points are the detections and the arrows are the sources for which only an upper limit, for the dust mass, could be found. The error bars are shown only for the detected disks, and show a high degree of uncertainty. As it can be seen from tab. 4.1 the star mass is not available for all the disks, six are missing.

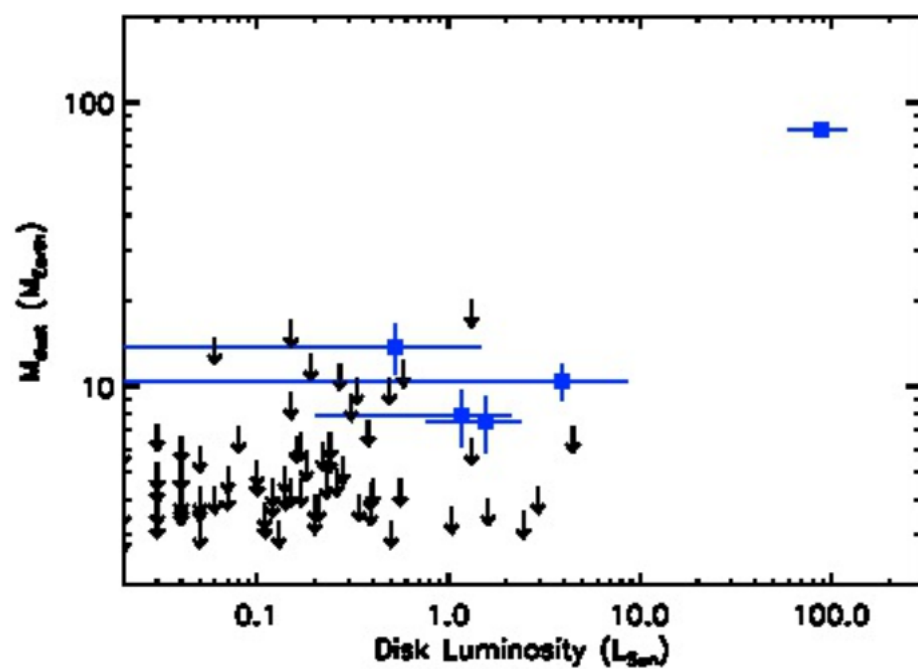


Figure 4.6: Plot showing the relation between the infrared disk luminosities (from Oliveira, 2013) and the dust masses. The blue points are the detections and the arrows are the sources for which only an upper limit, for the dust mass, could be found. The error bars are shown only for the detected disks.

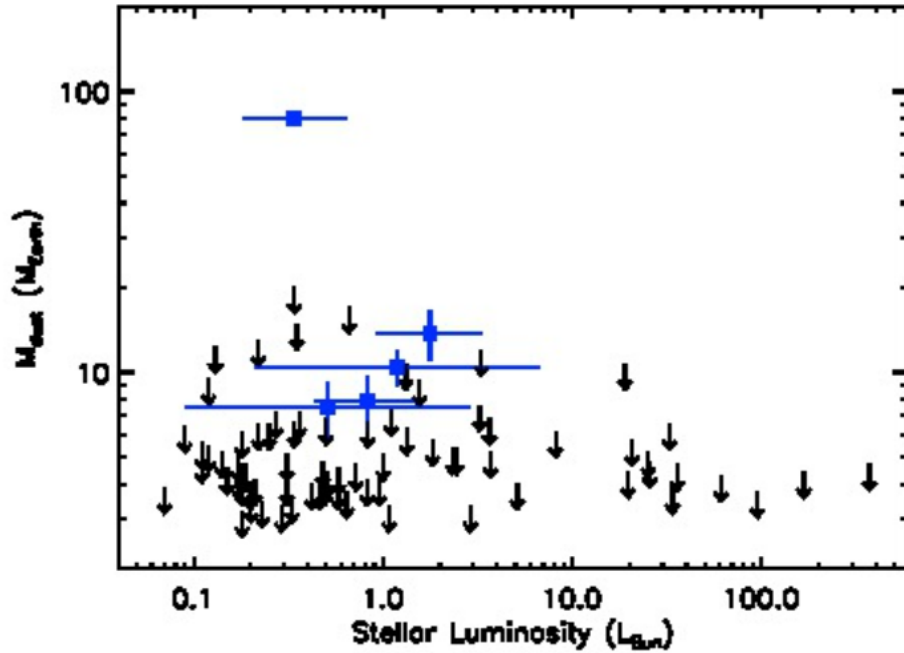


Figure 4.7: Plot showing the relation between the luminosity of the central stars (from Oliveira, 2013) and the dust masses. The blue points are the detections and the arrows are the sources for which only an upper limit, for the dust mass, could be found. The error bars are shown only for the detected disks.

luminosity vs the dust mass. In this plot all the detected disks are in a region close to the sun luminosity and it is possible to notice that all the upper limits decrease with increasing stellar luminosity. While this could be due to the lack of data for brighter stars, it could provide important information about the disk evolution: brighter stars have less massive disks. The previous statement can be interpreted as brighter stars heat more efficiently the dust in their disks, leading to higher temperatures and higher thermal speeds of the grains. When the thermal speed exceeds the escape velocity, determined by the gravity of the star, the dust grains are dissipated into space and the total dust mass is reduced.

Fig 4.8 is a plot relating the central star mass, x-axis, with the dust mass, y-axis. Here it is interesting to note that 4 out of 5 detections are in the range of 0.9-1.1 solar masses for the stellar mass and again going to higher values the upper limits decrease. The last plot in fig. 4.9 shows the stellar T_{eff} vs M_{dust} . It shows most of the point are in the 3000-4500 K interval and even here a trend is visible: hotter stars have less massive disks, similar to the behavior seen with the stellar luminosities.

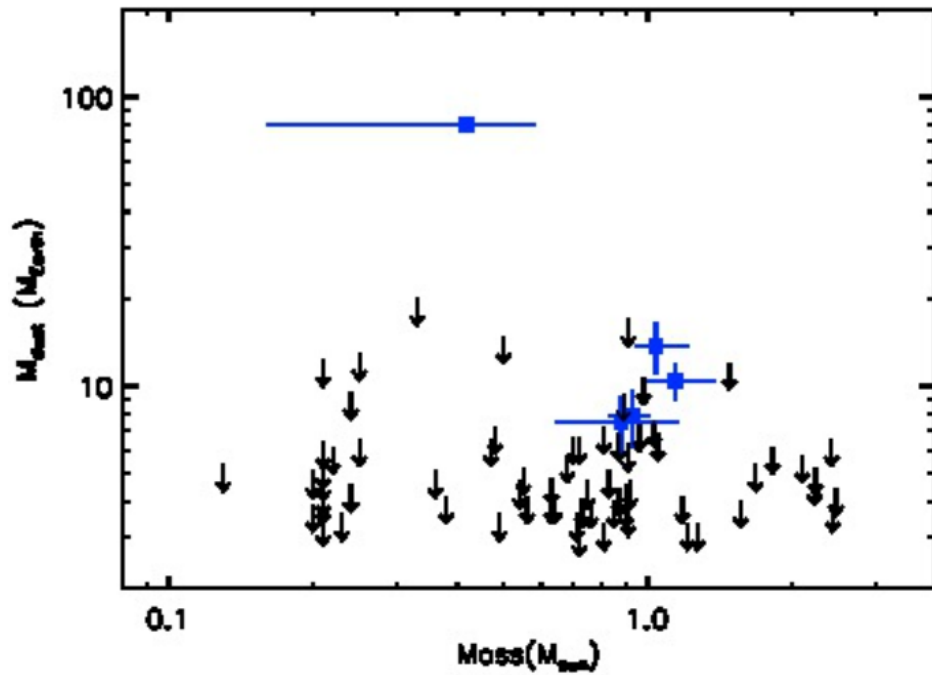


Figure 4.8: Plot showing the relation between the central stellar masses (from Oliveira, 2013) and the dust masses. The blue points are the detections and the arrows are the sources for which only an upper limit, for the dust mass, could be found. The error bars are shown only for the detected disks. As it can be seen from table 4.1 the star mass is not available for all the disks, six are missing.

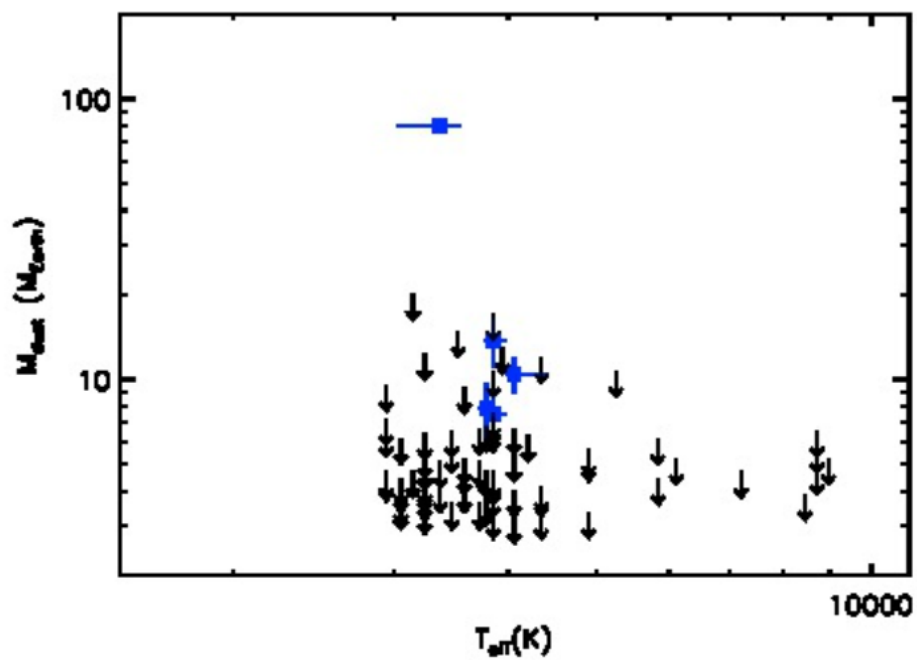


Figure 4.9: Plot showing the relation between the stellar effective temperatures (from Oliveira, 2013) and the dust masses. The blue points are the detections and the arrows are the sources for which only an upper limit, for the dust mass, could be found. The error bars are shown only for the detected disks.

Chapter 5

Conclusions

In this thesis I performed the calibration, using MIRIAD on the 35 CARMA tracks, taken at 3mm, of 81 young disks in the Serpens star forming region, and then separated the usable datasets from the “bad ” ones which were not used. From the calibrated datasets I extracted the maps, again using MIRIAD and the CLEAN algorithm, for the 81 observed YSOs of the survey. From each map I extracted the RMS(σ) and where there was a detection at $> 3\sigma$ the flux of the source using CASA and the UVFIT task of MMIRIAD. Using eq. 4.1 and the fluxes I derived from the previous step, I obtained the dust masses for the disks, or the upper limit to this mass. Only 5 disks were detected: ID 3 with a dust mass of 13.80 Earth masses, ID 7 with 7.54 Earth masses, ID 58 with 10.45 Earth masses, ID 60 with 7.90 Earth masses and the most massive ID 146 with 80.36 Earth masses. These masses can be translated in gas masses using the $M_{gas}/M_{dust} = 100$ ratio. Finally using the data from table 4.1 and IDL, I drew some plots in an attempt to find some relation between different properties. Unfortunately no conclusive evidence can be found due to the small number of detected disks, but some intriguing trends can be seen in the plots: no detections were found for high luminosity or massive central stars and older systems.

This work will be useful for guiding future SMA (Sub-Millimeter Array) observations of the same disks. These observations, thanks to the better sensibility of the SMA interferometer, will likely be able to achieve more detections or stricter upper limits to the dust mass in these disks and observing at the 1mm wavelength will give more information on the dust emission spectral index, which is tied to the size of the dust grains. This work will also give priority to the sources, for which, some emission was detected, but it was not bright enough to reach the 3σ limit, therefore to be considered a detection.

Bibliography

- [Herbig(1950)] Herbig, G. H. 1950, ApJ, 111, 11
- [Ricci et al.(2008)] Ricci, L., Robberto, M., & Soderblom, D. R. 2008, arXiv:0808.3336
- [Ney et al.(1973)] Ney, E. P., Strecker, D. W., & Gehrz, R. D. 1973, ApJ, 180, 809
- [Beckwith et al.(1990)] Beckwith, S. V. W., Sargent, A. I., Chini, R. S., & Guesten, R. 1990, AJ, 99, 924
- [McCaughrean & O'dell(1996)] McCaughrean, M. J., & O'dell, C. R. 1996, AJ, 111, 1977
- [O'dell & Wong(1996)] O'dell, C. R., & Wong, K. 1996, AJ, 111, 846
- [Dutrey et al.(1996)] Dutrey, A., Guilloteau, S., Duvert, G., et al. 1996, A&A, 309, 493
- [Simon et al.(2000)] Simon, M., Dutrey, A., & Guilloteau, S. 2000, ApJ, 545, 1034
- [Lada & Wilking(1984)] Lada, C. J., & Wilking, B. A. 1984, ApJ, 287, 610
- [Andre et al.(1993)] Andre, P., Ward-Thompson, D., & Barsony, M. 1993, ApJ, 406, 122
- [Andre & Montmerle(1994)] Andre, P., & Montmerle, T. 1994, ApJ, 420, 837
- [Shu et al.(1987)] Shu, F. H., Adams, F. C., & Lizano, S. 1987, ARA&A, 25, 23
- [Armitage(2013)] Armitage, P. J. 2013, Astrophysics of Planet Formation, by Philip J. Armitage, Cambridge, UK: Cambridge University Press, 2013,
- [Jackson(2008)] Jackson, N. 2008, Jets from Young Stars II, 742, 193

- [Gomez de Castro et al.(1988)] Gomez de Castro, A. I., Eiroa, C., & Lenzen, R. 1988, *A&A*, 201, 299
- [Gutermuth et al.(2008)] Gutermuth, R. A., Bourke, T. L., Allen, L. E., et al. 2008, *ApJ*, 673, L151
- [Bontemps et al.(2010)] Bontemps, S., André, P., Könyves, V., et al. 2010, *A&A*, 518, L85
- [Harvey et al.(2007)] Harvey, P., Merín, B., Huard, T. L., et al. 2007, *ApJ*, 663, 1149
- [Harvey et al.(2006)] Harvey, P. M., Chapman, N., Lai, S.-P., et al. 2006, *ApJ*, 644, 307
- [Oliveira et al.(2010)] Oliveira, I., Pontoppidan, K. M., Merín, B., et al. 2010, *ApJ*, 714, 778
- [Oliveira et al.(2009)] Oliveira, I., Merín, B., Pontoppidan, K. M., et al. 2009, *ApJ*, 691, 672
- [Oliveira et al.(2013)] Oliveira, I., Merín, B., Pontoppidan, K. M., & van Dishoeck, E. F. 2013, *ApJ*, 762, 128
- [Lee et al.(2014)] Lee, K. I., Fernández-López, M., Storm, S., et al. 2014, *ApJ*, 797, 76